

---

## Early Neoproterozoic oxygenation dynamics along the northern margin of the West African Craton, Anti-Atlas Mountains, Morocco

Chi Fru Ernest <sup>1,\*</sup>, Bankole Olabode <sup>2</sup>, Chraiki Ibtissam <sup>3</sup>, Youbi Nassreddine <sup>3</sup>, Millet Marc-Alban <sup>1</sup>, Rouxel Olivier <sup>4</sup>, El Albani Abderrazzak <sup>2</sup>, Bouougri El Hafid <sup>3</sup>

<sup>1</sup> School of Earth and Ocean Sciences, Centre for Geobiology and Geochemistry, Cardiff University, Cardiff CF10 3AT, Wales, UK

<sup>2</sup> University of Poitiers, CNRS IC2MP UMR, 7285 Poitiers, France

<sup>3</sup> DLGR, Department of Geology, Faculty of Sciences-Semlalia, Cadi Ayyad University, Marrakesh, Morocco

<sup>4</sup> Unité de Géosciences Marines, IFREMER, Z.I. Pointe du diable, BP 70, 29280 Plouzané, France

\* Corresponding author : Ernest Chi Fru, email address : [ChiFruE@Cardiff.ac.uk](mailto:ChiFruE@Cardiff.ac.uk)

[olabode.bankole@univ-poitiers.fr](mailto:olabode.bankole@univ-poitiers.fr) ; [ibtissamchraiki@gmail.com](mailto:ibtissamchraiki@gmail.com) ; [youbi@uca.ac.ma](mailto:youbi@uca.ac.ma) ; [milletm@cardiff.ac.uk](mailto:milletm@cardiff.ac.uk) ; [olivier.rouxel@ifremer.fr](mailto:olivier.rouxel@ifremer.fr) ; [abder.albani@univ-poitiers.fr](mailto:abder.albani@univ-poitiers.fr) ; [bouougri@uca.ma](mailto:bouougri@uca.ma)

---

### Abstract :

Emerging evidence suggests widespread ferruginous marine conditions promoted global seawater phosphate depletion and the maintenance of a low oxygen world at the start of the Neoproterozoic Era. However, the large-scale deposition of marine sedimentary Fe formations, as observed in the Paleoproterozoic, is rare in the early Neoproterozoic Era. We show that at the start of the Neoproterozoic, tidal flat and shallow marine environments along the northern passive margin of the West African Craton (WAC) were fully oxygenated and low in reactive Fe content, until an abrupt and prolonged episode of deep-sea hydrothermal activity overwhelmed the WAC margin with strongly reducing Fe-rich hydrothermal fluids. This unique incident is recorded in meter-thick and kilometer-wide shallow marine siliciclastic platform rocks estimated to be ~883 Ma old and containing average bulk Fe content >22 wt% in the Wanimzi Formation in the Moroccan Anti-Atlas Mountains. The abrupt and conformable contact of the Fe-rich succession with the Fe-poor lower and upper transition boundaries, together with geochemical data, suggest rapid initiation and termination of seawater fertilization by the hydrothermal fluids that formed the unmetamorphosed hematite-rich ironstones. Rare Earth Element (REE) and Fe-based redox reconstruction point to an aftermath coincident with a return to shallow siliciclastic marine habitats characterized by a low reactive Fe content and negligible hydrothermal intrusion, where aerobic microbial communities flourished in well-oxygenated waters. We propose that the early Neoproterozoic tectonic initiation of the breakup of the supercontinent Rodinia supplied large volumes of deep sea hydrothermal Fe, trace metals, and toxic metalloids like arsenic to shallow marine habitats along the WAC, resulting in rapid seawater deoxygenation.

---

**Keywords** : Siliciclastic iron formation, Tonian period, Ironstones, Hydrothermal activity, Rodinia supercontinent.

## 1. Introduction

It is widely accepted that Precambrian seawater Fe concentrations exerted a major control on early ocean chemistry, oxygenation of the atmosphere, climate, and the evolution of global biogeochemical cycles (e.g., Frei et al., 2008; Planavsky et al., 2010; Heimann et al., 2010; Halverson et al., 2011; Lyons et al., 2014; Brock et al., 2017; Hoffman et al., 2017; Reinhard et al., 2017; Song et al., 2017; Guilbaud et al., 2020; Heard and Dauphas, 2020). For instance, Fe mineral precipitation modulates the concentration of dissolved species in seawater, including macro- and micro-nutrient content (e.g., Dymek and Klein, 1988; Konhauser et al., 2002; Fischer and Knoll, 2009; Zegeye et al., 2012; Chi Fru et al., 2012, 2013, 2015a-b, 2016a-b; Large et al., 2015; Haugaard et al., 2016; Hoffman et al., 2017; Konhauser et al., 2017; Hemmingsson et al., 2018; Keyser et al., 2018; Mukherjee et al., 2019; Robbins et al., 2019; Heard and Dauphas, 2020).

As a consequence, throughout the Archean and for most of the Paleoproterozoic eon, considerable quantities of ferrous Fe oxidized out of seawater to form sizable Algoma type Fe formations containing >15 wt.% Fe in deep sea Archean volcanic centers and Superior type banded iron formations (BIF) on passive Paleoproterozoic sea margins (see Bekker et al., 2010 for a review). A systematic reduction in the deposition of Fe formations has been linked to the permanent appearance of free molecular oxygen in the atmosphere during the so called Great Oxidation Event (GOE) (Bekker et al., 2010; Lyons et al., 2014). This is thought to be the result of enhanced biotic and abiotic oxidation of soluble ferrous Fe to insoluble ferric Fe minerals using molecular oxygen as an efficient electron acceptor (Emerson et al., 2010; Chi Fru et al., 2012), accelerated precipitation of pyrite because of the intensification of microbial sulfate reduction as a result of GOE-induced rise in seawater sulfate concentrations and progressive weakening of hydrothermal activity through Earth history (e.g., Canfield, 1998; Bekker et al., 2010; Poulton and Canfield, 2011; Lyons et al., 2014).

Following the GOE, the oceanic redox structure differentiated into oxygen-rich shallow surface waters, mid-depth continental margin sulfide-rich (euxinic) waters, and deep ferruginous waters (e.g., Canfield, 1998; Rouxel et al., 2005; Poulton et al., 2011; Reinhard et al., 2013; Lyons et al., 2014; Dauphas et al., 2016; Mukherjee et al., 2019). Pyrite precipitated in the euxinic settings, while the upwelling and the mixing of the deep ocean ferruginous waters with the oxygenated chemocline and surface waters, shuttled silica and ferric Fe to the sea floor (Canfield, 1998; Fischer and Knoll, 2009; Poulton and Canfield, 2011; Reinhard et al., 2013).

Because of the high affinity of both pyrite and ferric Fe for trace elements, these important Fe minerals controlled the mobility and availability of trace elements in seawater through co-precipitation and adsorption reactions (e.g., Reinhard et al., 2013; Large et al., 2015; Mukherjee et al., 2019; Robbins et al., 2019). For example, the enrichment of Mo and As in euxinic marine sediments correlate with pyrite accumulation (Reinhard et al., 2013; Chi Fru et al., 2019) while rapid trace element removal from seawater by ferric Fe is observed in oxygenated environments where biological and abiobiochemical oxidation of ferrous Fe with oxygen occurs (Konhauser et al.,

2002; Chi Fru et al., 2012; Emerson et al., 2010) and in anoxic settings where phototrophic oxidation of ferrous Fe is prevalent (Thompson et al., 2019).

The ferric Fe particles can be reduced in the deep anoxic ocean and sediments by the dissimilatory Fe-reducing bacteria (DIR) using organic carbon and nitrate (Weber et al., 2006) and/or by sulfide (Poulton and Canfield, 2011) to recycle ferrous Fe and bound trace elements and nutrients back to seawater (e.g., Guilbaud et al., 2020). Consequently, Fe carbonates in ancient Fe formations are thought to record the respiratory activities of the DIR (e.g., Severmann et al., 2008; Heimann et al., 2010; Craddock and Dauphas, 2011). Because of the strong coupling between the oxidation state of Fe and seawater redox, the speciation of Fe mineral phases in primary marine chemical sediments has gained widespread application in the reconstruction of past seawater redox state from sedimentary rocks (Poulton and Canfield, 2005; Poulton et al., 2011; Sperling et al., 2015; Raiswell et al., 2018).

This study describes an early Neoproterozoic siliciclastic Fe formation deposited as part of a shallow marine environment along the northern margin of the West African Craton (WAC) in the Anti-Atlas belt of Morocco. We unravel how Fe was sourced from a deep-marine oxygen-starved, hydrothermally active ocean and mixed with oxygenated coastal shoreline waters to form the siliciclastic Wanimzi ironstones. We propose that this incident is linked to tectonic events that initiated the breakup of the supercontinent Rodinia and that this event had severe consequences for life and the oxygenation of affected shallow seawater masses along the WAC coast.

## **2. Geological setting**

The Proterozoic basement of the Anti-Atlas constitutes the northern margin of the WAC. It is overprinted by Pan-African-Cadomian events and bounded by two tectonic fault zones, represented by the Anti-Atlas major Fault (AAMF) and the High-Atlas South Fault (e.g. Leblanc & Lancelot, 1980; Saquaque et al., 1989; Bouougri, 2003; Ennih & Liegeois, 2008). The AAMF (e.g. Choubert, 1947; Leblanc and Lancelot, 1980; Saquaque et al., 1989) is a tectonic boundary separating the cratonic margin to the south from the ~770-

700 Ma island arc-related terrane to the north that was accreted onto the margin during Pan-African collisional events ~663-640 Ma (e.g. Leblanc et Lancelot, 1980; Saquaque et al., 1989; Bouougri, 2003; El Hadi et al., 2010; Thomas et al, 2004; Inglis et al., 2005; Triantafyllou et al., 2016; Fig. 1a).

The post-Eburnean craton margin strata of the Anti-Atlas, comprising of a volcano-sedimentary succession up to 2 km thick spanning the Upper Paleoproterozoic to Early Neoproterozoic time, crops out along the AAMF (Figs 1b). Based on radiometric data, the successions unconformably overlying the Eburnean basement (~2000-1800 Ma) is subdivided according to new radiometric data into three main tectono-sedimentary sequences spanning the Columbia and Rodinia supercontinent cycles (Letsch, 2018; Bouougri et al., 2020). The complete section is well exposed in the central part of the Anti-Atlas along the AAMF, with a tripartite subdivision into a Lower sedimentary ensemble, a Middle volcanic unit and an Upper sedimentary sequence (Bouougri and Saquaque, 2004). In previous works, and considering mainly the Pan-African tectonic features and the lack of any evidence for a Mesoproterozoic Grenvillian tectono-thermal event in the Anti-Atlas and in the WAC, the whole succession was assigned to the Neoproterozoic and to the Pan-African rifted-margin of the Anti-Atlas (Leblanc et Lancelot, 1980; Saquaque et al., 1989; Leblanc and Moussine-Pouchkine, 1994), formally named the Tizi n'Taghatine Group in its stratotype area (Bouougri and Saquaque, 2004). However, revised stratigraphic framework as well as new radiometric ages obtained from interbedded volcanic occurrences, mafic sills cross-cutting the lowermost part of the succession, and U-Pb ages from detrital zircons, provide evidence for two tectono-stratigraphic cycles of Upper Paleoproterozoic to possibly Mesoproterozoic pre-Pan-African and the Neoproterozoic Pan-African cycle (Letsch, 2018; Bouougri et al., 2020). The first cycle extends from the bottom to the Tasserda, Taghdout and Oumoula Formations. This is succeeded by the Neoproterozoic, subdivided into Tonian strata (~883 Ma) and the ~700 Ma Cryogenian Bleïda Formation, interpreted as rift-related and pre-collisional foreland basin successions, respectively (Bouougri et al., 2020).

The 883 Ma age is obtained from pyroclastic material lying directly above the Imi n-Tizi Formation (Bouougri et al, 2020; Fig. 2a). Gradual emergence of

volcanic activity and transition into the deposition of the mainly volcanic rocks in the Tachdamt Formation from the underlying Wanimzi Formation is indicated by the placement of interbedded pyroclastic flow beds in the underlying platform deposits. This kind of transition as well as evidence of feeder dykes cutting through the platform deposits, collectively suggest a Tonian age close to ~883 Ma. Moreover, by considering the maximum 500 m thickness of the platform deposits, low sedimentation rates of  $0.06 \text{ cm year}^{-1}$ , the lack of evidence for a time gap, and a high rate of compaction, deposition of the entire succession could not have exceeded a duration of ~5 million years (Bouougri et al., 2020). The platform deposits, including the Wanimzi Formation, are part of the start of a global Neoproterozoic cycle that triggered the breakup of the Rodinia supercontinent ~900 Ma (Bouougri et al., 2020).

In the studied area along the southern margin of the Siroua Inlier (Fig. 1b), the Pan-African rift-related succession of Tonian age is well exposed in the Agoumy section (Fig. 1b). The pre-rift sedimentary strata (Fig. 2a) in ascending order, include the Ifarkhs n' Tirsal, Wanimzi, Tamgarda, Agoumy and Imi n'Tizi Formations (Bouougri and Saquaque, 2004). This mixed siliciclastic-carbonate succession of shallow marine origin, is overlain by the syn-rift volcanic Tachdamt Formation. A new minimum age of ~883 Ma has been recently suggested for the pre-rift shallow marine mixed siliciclastic-carbonate deposits (Bouougri et al., 2020). Transition from the above shallow platform marine siliciclastic deposits to the overlying volcanic Tachdamt Formation shows no evidence of an erosional unconformity or time gap. Instead, a sharp contact characterized by remnants of pyroclastic occurrences atop of the Imi n'Tizi Formation, indicate stratigraphic continuity (Bouougri et al., 2020). The age of the platform deposit is thus considered very close to ~883 Ma and not older than ~900 Ma even when low sedimentation rates are considered for the platform wedge estimated to be ~500 m thick in the studied section. These shallow near-continental margin sedimentary rocks are thought to record a stable craton margin, which underwent major rifting and magmatic events that led to the breakup of Rodinia (Bouougri et al., 2020).

The lithology of the basal Paleoproterozoic Taghdout Formation in the studied section is dominated by carbonates and mixed siliciclastic-carbonate

rocks, while the early Neoproterozoic Wanimzi and Imi n'Tizi formations present fine-grained siliciclastic and heterolithic rhythmic beds, rich in sedimentary structures interpreted as reflecting a shallow shelf setting and the activities of ancient microbial mats (e.g., Bouougri and Saquaque, 2004; Bouougri and Porada, 2002). The heterolithic beds contain biolaminitic thin multilayered packages that formed on sand and as cm-thick planar laminated layers frequently disturbed by shrinkage cracks. A variety of mat-related structures previously identified in these heterolithic layers, in both the Wanimzi and Imi n'Tizi Formations, tend to be associated with reticulate patterns and microbial shrinkage cracks (Bouougri and Porada, 2002).

The studied Fe oxide-bearing Wanimzi Formation is a ~120 m thick siliciclastic unit dominated by heterolithic deposits showing an overall coarsening and shallowing upward trend (Fig. 2). Sedimentary features indicate a depositional setting in a storm and wave dominated shallow marine ramp (Bouougri and Saquaque, 2004). According to sand-mud ratio and facies features, three parts can be distinguished within this formation. These consist of (i) a lower mudstone and fine grained siltstone deposited below storm wave base (SWB), (ii) a middle heterolithic deposit including beds with hummocky cross stratification (HCS) indicating deposition above SWB in an outer offshore transition zone, and (iii) an Upper sand dominated sequence with amalgamated sandstone beds containing HCS and swaley cross-stratification (SCS), indicating deposition in the inner part of the offshore transition to a lower shoreface zone. The middle part contrasts clearly with other deposits and shows a dense red color related to Fe enrichment.

### **3. Methods**

#### *3.1. Sampling and sample preparation*

In the Agoumy area (Fig. 2b), fresh unweathered samples were collected at two key stratigraphic units from the Wanimzi Formation, with focus on the undescribed Wanimzi ironstones (Fig. 3) and reference microbial laminated samples from the overlying Imi n'Tizi Formations (Fig. 4). The Wanimzi Formation was sampled at 5-10 cm intervals at 30°30'0.58"N, 7°41'51.47"W and 30°29'57.84"N, 7°41'48.08"W (Fig. 3a-b&d). These well-exposed

outcrops (Fig. 3a-d) can be seen using satellite imagery to be laterally exposed for at least ~4 km.

Three reference carbonate samples were also collected from outcrops of the underlying older Paleoproterozoic (>1640 Ma) Eburnean basement at the Taghdout Formation and four from the well preserved stromatolite-rich siliciclastic rocks of the uppermost Imi n'Tizi Formation (Fig. 4a) described in Bouougri et al. (2002, 2007). The Taghdout carbonates and the Imi n'Tizi silicate rocks were sampled to provide Fe-poor references for comparison with the Fe-rich lithologies and to enable the interpretation of the transitional events that led to the onset and termination of the deposition of the Wanimzi ironstones. Representative stromatolitic units sampled from the Imi n'Tizi Formation consist of twisted biolaminations (S1), horizontal beds with no laminations (S2), consistent millimeter-thick bands (S3) and flat visible horizontal biolaminations (S4). Samples were collected for redox reconstruction, thin-section petrography, mineralogy, trace element (TE) and rare earth element (REE) analyses. C and Fe isotope measurements.

### *3.2. Petrography and mineralogy*

Before analysis, samples were shaved with a saw and exposed surfaces in contact with the atmosphere discarded. Polished thin-sections were prepared using standard rock-polishing laboratory procedures in the School of Earth and Ocean Sciences, Cardiff University. Portions of identical shaved thin-sectioned rock pieces were pulverized to a fine powder for geochemical analysis using a jaw crusher and by disc milling. Polished thin-sections for representative samples were examined for mineralogy and textural relationships under reflected and transmitted light microscopy using a Nikon ECLIPSE E600 POL microscope equipped with a Nikon Digital Sight DS-U1 camera at the University of Poitiers, France. Whole rock X-ray diffraction (XRD) mineral analyses were performed on powdered samples with a Bruker D8 ADVANCE diffractometer using CuK $\alpha$  radiation operating at 40 Kv and 40 mA and step size of 0.025/s between 2-65 °2 $\theta$  angular ranges.

### *3.3. Trace and Rare Earth Element analysis*

Bureau Veritas<sup>®</sup> (Vancouver, Canada) procedure code LF100-EXT was used to measure the concentration of 45 TEs and REEs in 0.2 g powdered samples. The samples were digested by lithium borate ( $\text{LiBO}_2/\text{Li}_2\text{B}_4\text{O}_7$ ) fusion and solutions analyzed by Inductively Coupled-Mass Spectrometry (ICP-MS). Lithium borate fusion is an aggressive chemical digestion process that effectively dissolves most refractory and resistant mineral phases, ensuring complete dissolution of powdered samples. Total Fe was measured by UV-Vis spectrometry using Stokey's ferrozine test as part of the Fe speciation protocol described in Poulton and Canfield (2004) and in section 3.4. Post Archean Australian Shale (PAAS) was used for REE+Y normalization (McLennan, 1989) and REE+Y anomalies are calculated as described previously (Bau and Dulski et al., 1996; Planavsky et al., 2010).

#### 3.4. Fe-based redox reconstruction

Redox reconstruction was obtained by application of the widely used Fe-based methodology for the reconstruction of bottom water redox conditions in modern and ancient siliciclastic and carbonate depositional environments habitats (Poulton and Canfield, 2005; Clarkson et al., 2014; Raiswell et al., 2018). This method allows the allocation of the Fe mineral phases into seven operational pools, divided into highly reactive ferric Fe and pyrite Fe phases ( $\text{Fe}_{\text{HR}}$ ), poorly reactive sheet silicate Fe and Fe in unreactive silicate (Poulton and Canfield, 2005). Samples were screened to contain >0.5 wt% Fe – a minimum threshold recommended to correct for variations in sedimentary Fe concentrations and dilution by detrital materials (Poulton and Canfield, 2005; Clarkson et al., 2014; Raiswell et al., 2018).

#### 3.5. Carbon and oxygen isotopes

Organic carbon ( $\text{C}_{\text{org}}$ ), carbonate carbon ( $\text{C}_{\text{carbonate}}$ ) and carbonate O isotopes ( $\text{O}_{\text{carbonate}}$ ) were co-measured on a Thermo Delta V Advantage mass spectrometer. The instrument is connected to a Thermo gasbench II for headspace sampling ( $\text{C}_{\text{carbonates}}$ ), while a Thermo Flash EA with Conflo III allows for the combustion of organic samples. The  $\delta^{13}\text{C}$  and  $\delta^{18}\text{O}$  are reported in the delta notation using the Vienna-Pee Dee Belemnite (VPDB) standard. The

$C_{\text{org}}$  and inorganic carbon content was estimated from a regression equation for signal intensity against the amount that was established for standard materials with known composition. Powdered samples were weighed into septum vials flushed with helium, acidified with 99 % orthophosphoric acid, and left to react for 24 hours at 60 °C to ensure complete reaction of dolomite. The long-term precision of an in-house Carrara marble standard has been estimated to 0.05 ‰ for both  $\delta^{18}\text{O}$  and  $\delta^{13}\text{C}$  (1sd). To eliminate inorganic carbon, prior to measuring  $C_{\text{org}}$  concentrations and  $\delta^{13}\text{C}_{\text{org}}$  isotopic distribution, samples were acidified in 10 % HCl and reaction left for two days. Residual acids was removed by washing the treated samples three times with ultrapure double distilled water. Sixty to eighty mg of samples were analysed for  $C_{\text{org}}$ . The total  $C_{\text{org}}$  analysed was as low as 10  $\mu\text{g}$  because of low  $C_{\text{org}}$  content. Three standards were used to calibrate the accuracy of these small sample concentrations: IAEA-CH6 [ $\delta^{13}\text{C}=-10.449$  ‰], IAEA-600 [ $\delta^{13}\text{C}=-27.771$  ‰], and an in-house caffeine [ $\delta^{13}\text{C}=-33.30$  ‰]) and were dissolved in de-ionised water to improve homogeneity and to allow accurate dosing of small aliquots using a micropipette. Results for IAEA-CH6 and the in-house caffeine were used to estimate a correction function for sample size and size-dependent 2-point normalisation, which was applied to IAEA-600 as the independent standard. The resultant precision is dependent on sample size. The long-term precision for  $\delta^{13}\text{C}$  was 0.09 ‰ (1sd) for routine samples containing  $\geq 100$   $\mu\text{g}$  C. However, the standard deviation increases with decreasing sample size, to 0.38 ‰ for aliquots with 10 - 30  $\mu\text{g}$  C as measured for the present study (IAEA-600, N=15).

### 3.6. Fe isotopes

Samples were dissolved by standard acid digestion using concentrated HF, HNO<sub>3</sub>, and hotplates in acid washed Teflon beakers, and purified through polypropylene pipette tips chromatographic columns containing a 500  $\mu\text{l}$  AG1-X4 anion exchange resin (Millet et al., 2012). Fe isotopes were measured at IFREMER, France, on a Thermo Scientific Neptune MC-ICP-MS set on medium or high-resolution mode as described in Rouxel et al. (2018). Analysis included sample-standard bracketing and internal normalization using Ni with a known isotope ratio and an internal precision of 0.04-0.09‰

(2sd) for 100 ng of recovered Fe (Rouxel et al., 2018). Data are reported as  $\delta^{56}\text{Fe}$  and  $\delta^{57}\text{Fe}$  ratios in parts per thousand deviations from the IRMM-014 standard. More than 50 replicates of the Hawaiian basalt internal standards BHVO-1 and BHVO-2 using this method yielded average  $\delta^{56}\text{Fe}$  values of  $0.09 \pm 0.07\text{‰}$  (Rouxel, 2018).

## 4. Results

### 4.1. Field observations and sedimentary features

The Fe-rich layers in the Wanimzi Formation often occur as oxidized red to purple cm-thick beds alternating with heterolithes and thin storm beds with HCS (Fig. 3a-c). In the lower part of Wanimzi Formation (Fig. 2b, 3d), several isolated decimeter-thick storm beds of Fe-rich sandstones were observed, some of which preserve artisanal digging trenches running parallel to the mineralized layers. The heterolithic beds are composed of silt, sand, and microbial biolaminated layers similar to the overlying Fe-poor Imi n'Tizi Formation (Fig. 4), indicating deposition of both successions above a storm wave base, in a shallow marine setting. Well-developed and previously described siliciclastic stromatolites, marked by prominent flat to large domal shaped morphologies (Bouougri and Porada, 2011), appear in the Imi n'Tizi fine-grained siliciclastic Formation (Fig 4g-h).

Several mat-related structures dominated by Kinneyia-type wrinkled structures, ripples, spindle-shaped and sinusoidal cracks, and sandstone chips were recognized within the heterolithic facies in the Wanimzi and Imi n'Tizi Formations (Fig. 4). The Kinneyia-type wrinkled structures in both formations occur on the upper surfaces of sandstone beds, and are characterized by mm-thick structures twisted into flat-top crests separated by round bottom troughs and pits that are comparable in size (Fig. 4c). Ripple marks on the top of several sandstone beds (Fig. 4a-b) are colonized and stabilized by thin or thick microbial mat layers (Bouougri and Porada, 2002). Spindle-shaped and sinusoidal cracks (Fig. 4d), equally abundant in the Wanimzi and Imi n'Tizi Formations, were associated with mm-laminated argillite, sandstones and silty sandstones that are sometimes formed on the upper surfaces of sandstone beds free of mud trappings (Fig. 4e). These structures present a great variety in size and shape, including sub-circular,

crescent-shaped and sinusoidal cracks observed on the upper bedding surfaces of fine-grained quartzite and siltstone layers. Structures related to microbial mat colonization and upper veneer stabilization of sand bedding surfaces occur as current deformation features and flat microbial sand clasts (Fig. 4e-f). The association of these features with large ripple slabs made up of sandstone confirms the deposition of the Imi n'Tizi Formation in a shallow marine environment. Horizons with sandstone chips and characterized by well-rounded to ellipsoidal flat-shaped features appear abundantly in the basal units of the medium to fine-grained quartzite layers.

Beginning with the microbial mat-rich Imi n'Tizi Formation that marks the top of the studied package, the layers are composed of two distinct sediment types, typified by sharp coarse and fine-sediment layers (Fig. 5a-b). The siliciclastic stromatolites consist of mat-growth structures made up predominantly of moderately compacted and well-sorted quartz-dominated silty-sandstone layers alternating thin mud shale laminae, consisting of micas and dominated by muscovite and illite (Fig. 5a-b; Table 1; Appendix A-B). The quartz coarse grains are detrital while the fine-grained layers have been suggested to be fossil remains of ancient microbial mat layers according to several mat-related features preserved on bedding surfaces (Bouougri and Porada, 2002). This simple repetitive architecture of coarse siliciclastic layers alternating with thinner fine-grained siliciclastic beds was observed on all sections investigated. Well-sorted, rounded, angular to sub-angular, silt-sand-sized quartz grains cemented in an Fe-rich matrix, are a unique characteristic and distinguishing hallmark of the Wanimzi Formation (Fig. 5c-f).

#### *4.2. Mineralogical characterization*

Thin section analysis of the Fe-rich lithologies in the Wanimzi Formation (Fig. 5) is consistent with the mainly siliciclastic composition of near continental margin Neoproterozoic deposits in the Moroccan Anti-Atlas Mountains. Although hematite and quartz are present in all lithologies, their predominant character is restricted to the Wanimzi ironstones (Appendix C-E & H-J), while quartz predominates the stromatolitic lithologies of the Imi n'Tizi Formation (Appendix A-N). The Taghdout Formation consists primarily of ooid-peloid grainstone cemented in a mainly quartz-carbonate matrix composed of

calcite, dolomite, minute hematite concentrations, feldspars, and illite/mica clays (Fig. 5g-i; Appendix F,G, L). The ooids are made of microcrystalline calcitic laminae with radially arranged calcite crystals and dark Fe enriched thinner laminae. Relics of oolites were identified showing the dissolution of the original structure and its replacement by drusy calcite crystals, indicating a neomorphism process (Fig. 5g-i; Appendix F,G, L).

#### 4.3. Trace element (TE) geochemistry

Out of the 45 elements analyzed, Fe is the most enriched across all lithologies (Fig. 6; Table 2). Co, V, U, As, Sb are pronounced in the ironstones which record varying Cu enrichment and Mo depletion compared to average concentrations in the siliciclastic stromatolitic and carbonate-rich rocks (Table 2; Fig. 6a-d). Cd was below the detection limit of 0.1 ppm in both the siliciclastic stromatolitic and hematite-rich rocks while averaging 0.37 ppm in the underlying carbonate-rich facies. Average As concentrations in the Wanimzi ironstones were 18.2, 8.8, and 19.4 times in excess of those measured in the overlying siliciclastic facies, the underlying siliciclastic carbonates and average upper continental crust values, respectively. These values were much lower for the siliciclastic and carbonate lithologies relative to the upper continental crust by a factor of 1.1 and 2.2, respectively. As and Sb expressed similar curves in all samples (Fig. 6a&d). Fe concentrations of up to 61.7%, averaging 22.4% (n=18) (Table 2) qualify the Wanimzi ironstones as an Fe formation based on the definition of a chemical sedimentary sequence containing >15% Fe (see for example Bekker et al., 2010).

The average Fe content in the ironstone lithologies are up to a factor of 34, 21, and 64 in excess of the average concentrations in the representative samples from the reference siliciclastic stromatolite-rich Imi n'Tizi Formation, the Taghdout siliciclastic carbonate facies, and the upper continental crust average reported by McLennan (2001), respectively (Table 2). Moreover, Fe and quartz are often inversely related in the Fe-rich rocks (Fig. 6e), but Fe remained generally below 1.0 wt.% in the stromatolitic and carbonate-rich layers. Zn/Co ratios largely decreased from the carbonates through to the overlying Neoproterozoic siliciclastic stromatolitic succession (Fig. 6f). Mo/W

ratios are generally low (Fig. 6g). Th/U ratios are relatively low in the Fe-rich sequences compared to the reference overlying and underlying Fe-poor samples (Fig. 6h).

#### 4.4. Carbon content, and carbon and oxygen isotope distribution

$C_{org}$  concentrations are generally low, ranging from 0.01 to 0.06 wt% across the sequence, with the highest values associated with the Taghdout carbonates (Fig. 6i; Table 3). The average value of  $C_{org}$  is  $0.02 \pm 0.0008$  wt%,  $0.05 \pm 0.012$  wt%, and  $0.01 \pm 0.004$  wt% in the ironstones, carbonates, and stromatolitic mats, respectively. The isotopic distribution of  $\delta^{13}C_{org}$  range from  $-33.03\text{‰}$  to  $-22.93\text{‰}$ , averaging  $-29.8 \pm 2.22\text{‰}$ ,  $-27.42 \pm 0.99\text{‰}$ , and  $-29.49 \pm 1.85\text{‰}$  in the Fe-rich, the carbonates, and the stromatolitic lithologies, respectively. The lowest and highest single  $\delta^{13}C_{org}$  values are recorded in the Fe-rich rocks (Fig. 6j; Table 3), while the rare occurrence of carbonates in the Fe-rich rocks is consistent with XRD data except for sample AG14 with a carbonate concentration of 0.21 wt% and associated  $\delta^{13}C_{carbonate}$  and  $\delta^{18}O_{carbonate}$  values of  $-8.72\text{‰}$  and  $-12.79\text{‰}$ , respectively, (Table 3). The carbonate-rich lithologies have high carbonate concentrations between 50 and 75 wt%, with measured  $\delta^{13}C_{carbonates}$  and  $\delta^{18}O_{carbonate}$  values ranging from  $-0.77\text{‰}$  to  $0.11\text{‰}$  (average =  $-0.28 \pm 0.45\text{‰}$ ) and  $-14.5$  to  $-13.28\text{‰}$  (average =  $-14.03 \pm 0.65\text{‰}$ ), respectively (Table 3).

#### 4.5. Rare Earth Elements (REEs)

Post Archean Australian Shale (PAAS) normalized REE patterns are generally similar for the siliciclastic biolaminites and Taghdout carbonate lithologies, but largely different for the Wanimzi ironstones (Fig. 7a-c). The three facies types show pronounced seawater influences consistent with LREE depletion, strong Ce depletion and sporadic Y enrichment (Table 4; Fig. 7). There is pronounced enrichment of Nd, Sm, Eu, Gd, Tb, and Dy relative to Ho and Tm depletion in some of the ironstone lithologies that distinguishes the ironstone deposits from the underlying and overlying Fe-poor rocks (Fig. 7). REE cross plots, including Zr and Th, show selective enrichment patterns that may be related to provenance (Fig. 8).

PAAS normalized Eu anomalies corrected for anomalously high sedimentary Gd concentrations,  $(Eu/Eu^*)_{SN1}$ , averaged ( $\pm$ standard deviation from the mean)  $1.13\pm 0.09$ ,  $1.24\pm 0.08$ , and  $1.04\pm 0.03$  for the Taghdout carbonate facies, the ironstones, and the siliciclastic stromatolitic rocks, respectively (Fig. 9a). When corrected for elevated Tb,  $(Eu/Eu^*)_{SN2}$  averaged  $1.14\pm 0.08$ ,  $1.16\pm 0.09$ , and  $1.09\pm 0.08$  for the ironstones, the siliciclastic stromatolitic and Taghdout carbonate facies, respectively, with corresponding averaged LREE/HREE ratios of  $3.37\pm 0.59$ ,  $2.12\pm 1.23$ , and  $3.96\pm 0.90$ , respectively. The average Y/Ho ratios for the ironstones, the siliciclastic biolaminites, and Taghdout carbonate facies are  $27.45\pm 1.14$ ,  $28.40\pm 2.80$ , and  $27.50\pm 1.78$ , respectively (Fig. 9b), which are relatively close to a typical crustal and clastic sediment molar ratio of 28, suggesting a strong siliciclastic detrital influence on the REE composition of the sediments. The average Y/Ho ratios reflect lowered reactivity of Y by the presence of siliciclastic material, which as expected, tends to be lower compared to non-siliciclastic deposits (McLennan, 1989; Bau et al., 1997; Planavsky et al., 2010; Halverson et al., 2011).

$La_{SN}$  anomalies  $(La/Yb)_{SN}$  are typically positive with average values of  $1.07\pm 0.27$ ,  $0.85\pm 0.62$ , and  $0.95\pm 0.26$  for the Taghdout carbonates, the Fe-rich deposit and the siliciclastic mats, respectively (Fig. 9c), compared to Precambrian Fe formation values that are typically vary between 0.10 and 0.89 (Planavsky et al., 2010).  $(Tb/Yb)_{SN}$  average values are  $0.96\pm 0.10$ ,  $1.68\pm 0.67$ , and  $0.79\pm 0.09$  whereas  $(Pr/Yb)_{SN}$  have averages of  $0.90\pm 0.20$ ,  $0.84\pm 0.51$ , and  $0.91\pm 0.24$  for the Taghdout carbonates, the Fe-rich deposit and the siliciclastic mats, respectively (Fig. 9d). The  $(Sm/Yb)_{SN}$  ratios averaged  $0.98\pm 0.096$ ,  $1.18\pm 0.31$ , and  $0.77\pm 0.14$  for the Taghdout carbonates, the Fe-rich deposits and the siliciclastic biolaminites, respectively (Fig. 9e), while the  $(Eu/Sm)_{SN}$  averages for the Taghdout carbonates, the Wanimzi ironstones and the siliciclastic biolaminites are  $0.96\pm 0.096$ ,  $1.14\pm 0.31$ ,  $1.06\pm 0.06$  respectively (Fig. 9f).  $Gd_{SN}$  anomalies  $[(Gd/Gd^*)_{SN} = Gd_{SN}/(0.33Sm_{SN}+0.67Tb_{SN})]$  have average values of  $0.92\pm 0.02$ ,  $1.13\pm 0.13$ , and  $0.91\pm 0.06$  for the Taghdout carbonates, the ironstones and the siliciclastic stromatolites, respectively (Fig. 9g). The strong positive  $Gd_{SN}$

anomalies for the Wanimzi Fe-rich deposit is consistent with those found in many Precambrian IFs.

#### 4.6. Redox reconstruction

With the exception of two samples, the three successions (Fig. 9a) display pronounced true cerium anomalies ( $Ce/Ce^*$ ). However, redox reconstruction using Fe-based redox proxy points to mainly ferruginous and anoxic bottom water during the deposition of the ironstones and the carbonate lithologies, with full water column oxygenation limited to the Fe-poor stromatolitic reference rocks (Fig. 10b-c).

#### 4.7. Fe Isotopes

Bulk  $\delta^{56}Fe$  distribution in the stromatolitic and the Wanimzi Fe-rich lithologies range from 0.45‰ to 0.61‰ and -0.41‰ to 0.25‰ with means of 0.52‰ and -0.03‰, respectively (Fig. 11a-b; Table 3). With a fractionation factor of 0.55‰ (i.e.,  $\Delta^{56}Fe = \delta^{56}Fe_{\text{stromatolitic unit}} - \delta^{56}Fe_{\text{Fe-rich units}}$ ), the data show that the siliciclastic stromatolitic rocks are  $\delta^{56}Fe$  enriched compared to the Fe-rich units. At <5 wt.% Fe concentration,  $\delta^{56}Fe$  values become increasingly positive, and at >5 wt.% Fe concentration, they switch towards being more negative, with the exception of sample AG08 and AG12 (Fig. 11c).

## 5.0. Discussion

### 5.1. Sediment mineralogy and paragenesis

The primarily siliciclastic composition of the three studied successions, differing only in their Fe, quartz, and carbonate contents, suggests formation of these deposits in a stable shallow marine platform environment (e.g. Schofield et al., 2006; Ennih and Liegeois, 2008; Jessell et al., 2016). The heterolithic bedding planes and the abiotic and biotic structures common in both the Wanimzi and the Imi n'Tizi Formations are consistent with their previously described deposition in a shallow marine setting marked by intermittent desiccation intervals characterized by shrinkage cracks (Bouougri and Porada, 2002). The high siliciclastic content of the studied successions characterized by well-sorted, angular, rounded grains that range in size from

fine to coarse clasts, and the presence of extensive ripple marks and desiccation cracks, are typical features of peritidal environments.

The studied ironstone facies lack typical mineral assemblages associated with late stage diagenesis and metamorphism. Secondary mineral phases such as Fe carbonates, often interpreted to be products of reductive transformation of ferric Fe during burial diagenesis and lithification, could not be detected by XRD, consistent with a low Fe carbonate signal obtained by the sequential Fe extraction method. Collectively, this observation suggests that the emergence of more energetic electron donors such as nitrate in post-GOE seawater (e.g., Stüeken et al., 2016) may have subdued DIR bacteria activity relative to the Archean. For instance, Archean IFs record high Fe carbonate concentrations compared to the simpler and mainly hematite-rich mineralogy of Proterozoic and Phanerozoic IFs (Dekker et al. 2010, Chi Fru et al., 2013; Lechte et al., 2018). Negligible post-depositional transformation is further evidenced by the mainly hematite cement considered to reflect primary to early diagenetic sedimentary features in Fe formations (Chi Fru et al., 2013, 15b, 2018a; Sun et al., 2015; Halverson et al., 2011). Mineralogical and microscopic analyses, combined with Fe speciation data, suggest primary and diagenetic pyrite deposition is imperceptible across the succession and no evidence was found to support pyrite oxidation as the source of ferric Fe in the rock. Significant sulfide production is expected to inhibit ferric Fe deposition through rapid chemical reaction with ferrous Fe, combined with abiotic ferric Fe reduction by sulfide (Wensheng and Millero, 1996; Poulton et al., 2004). The floating of silty grains in the Fe-rich cement and the occurrence of hematite, together with indiscernible grain replacement and transformation of the primary hematite (Figs. 5c-d; Appendix C-D), point to minimal compaction diagenesis and to the syngenetic origin of hematite in the Fe-rich Wanimzi ironstones. Combined with trace element and REE analyses and as discussed further below, collectively the data do not support a subterranean or potential groundwater supply of Fe to the basin during the formation of the Wanimzi ironstones.

The  $\delta^{13}\text{C}_{\text{org}}$  values, supported by the preservation of stromatolitic mats, suggest all three successions were associated with photosynthetic activity. The similar average  $\delta^{13}\text{C}_{\text{org}}$  values for the Fe-rich and stromatolitic layers

differ from the underlying Taghdout carbonates by 2.4‰ and 2.0‰, respectively. We propose that similar carbon cycling processes were involved in the deposition of the early Neoproterozoic Waminzi Fe-rich units as in the siliciclastic stromatolitic rocks. The very negative  $\delta^{13}\text{C}_{\text{carbonate}}$  values of the underlying Taghdout Formation suggest negligible burial of photosynthetic  $\text{C}_{\text{org}}$ , which is demonstrated by the low  $\text{C}_{\text{org}}$  concentrations recorded at this time. It is also possible that the extreme negative  $\delta^{13}\text{C}_{\text{carbonate}}$  values reflect authigenic activity of the methane oxidizing bacteria (Schrag et al., 2013). There is no evidence in our dataset to suggest carbonate weathering as a mechanism that produced the large negative  $\delta^{13}\text{C}_{\text{carbonate}}$  excursion (Shields et al., 2017).

## 5.2. Hydrothermal versus seawater contribution

### 5.2.1. Insights from REE Systematics

REEs are reliable source tracers of sedimentary deposits. Being largely immobile in aqueous solution, they tend to behave conservatively during sediment formation (Taylor and McLennan, 1985). For example, La/Sm and Gd/Yb ratios normalized to upper continental crust values are frequently used as sediment source indicators (e.g., Wani and Mondal, 2011). Shale normalized Ce ( $\text{Ce}_{\text{SN}}$ ) depletion is assumed to be a seawater and redox proxy, and  $\text{Eu}_{\text{SN}}$  enrichment, a hydrothermal marker as well as a weathering proxy (Bau and Dulski, 1996; Singh and Rajamani, 2001; Shields et al., 2004; Bau and Koschinsky, 2009). The depletion of  $\text{Ce}_{\text{SN}}$  across the studied succession thus provides significant evidence for major seawater involvement in the origin of the studied facies (e.g., Tostevin et al., 2016). This conclusion is corroborated by independent sedimentological evidence that has long alluded to a marginal sea setting for the studied facies (e.g., Hefferan et al., 2000; Bouougri and Saquaque, 2000, 2004; Ennih and Liégeois, 2001; Thomas et al., 2004; Bouougri and Porada, 2002, 2010; Bouougri et al., 2020).

The statistically supported positive correlations between Nd (usually of hydrothermal or seawater origin) and Pr and Th (both often depleted in hydrothermal fluids) and Ce (of either hydrothermal or seawater provenance) and Pr (Bau and Dulski, 1996, 1999; Planavsky et al., 2010), suggest a

predominantly seawater origin for Ce. The positive correlation between Ce and the non-hydrothermal Pr, combined with the pronounced seawater  $Ce_{SN}$  signal, provide robust support for the latter proposition. Similarly, the lack of correlation amongst the three REEs - Nd vs Ga and Nd vs Eu (Fig. 8d, h), which are commonly enriched in hydrothermal fluids (German and Seyfried, 2014), again suggest REE contributions from seawater, probably as adsorbates of the abundant siliciclastic detritus. The latter proposal is consistent with the strong positive correlations of Ce vs. La and Ce vs. Nd (Fig. 8e-f), which hint that both La and Nd may be of a strong seawater origin. Typically,  $Eu_{SN}$  enrichment is attributed to hydrothermal activity (e.g., Douville et al., 2002; Tivey, 2007; Planavsky et al., 2010; German et al., 2014). However, the subtle positive enrichment of  $Eu_{SN}$  in the samples coupled to the moderate positive correlation between Eu and the non-detrital Zr (Fig. 8l), point to up to 58 % of Eu being associated with the siliciclastic material.

Increasing depletion of HREEs relative to LREEs, typically interpreted as evidence for hydrothermal influence, has been reported for Fe formations across Earth history (e.g., Planavsky et al., 2010; Bau, 1996; Ganno et al., 2017). For example, hydrothermal fluids emitted by modern deep-sea vents are generally enriched in LREEs (Mitra et al., 1994; Bau and Dulski, 1999; Craddock et al., 2010), whereas enrichment of HREEs relative to LREEs is a common feature of the modern oxygenated seawater (e.g., Bau et al., 1997; Bolhar et al., 2007) but has also been recorded in hydrothermal fluids in a few cases (e.g., Klinkhammer et al., 1994; Douville et al., 1999). Non-siliciclastic Precambrian Fe formations with pronounced HREE enrichments also contain positive (Eu, La, Y and Ga) $_{SN}$  anomalies (Bau and Dulski, 1996). We propose that the fluctuating LREE/HREE ratios recorded in the Wanimzi ironstones reflect varying degrees of the mixing of hydrothermal fluids with seawater.

Because the entire sample set is characterized by detrital loading, the unique trends in the ironstones cannot be related to an anomaly attributable to detrital contamination relative to the reference underlying and overlying rocks, which are also composed of siliciclastic detritus. We therefore interpret the above observations to reflect long distance transportation and thorough mixing of the Fe-rich fluids with seawater, followed by delivery and deposition on the margin of the WAC (Fig. 13). The data also imply that the seawater

chemical conditions on the WAC margin were radically different from those at the source and during transportation, to enable the quantitative precipitation of dissolved Fe from seawater and transformation into ironstone.

### 5.2.2. *Insights from trace element systematics*

The Wanimzi Fe-rich lithologies are enriched in key redox sensitive elements, such as As, V, Co, Sb, and Fe, that are typically concentrated in submarine hydrothermal fluids by up to eight times relative to modern seawater concentrations (e.g., Douville et al., 2002; Tivey, 2007; German and Seyfried, 2014). This would have been more significant in the Precambrian oceans that experienced much higher levels of hydrothermal activity. For example, Fe supplied by submarine hydrothermal fluids is suggested to be a major source of Fe to Precambrian seawater (see for example Bekker et al., 2010), with values in excess of  $10^3$  ppm reported for fluids from present-day mid-ocean spreading ridges (Tivey et al., 2007).

Evidence shows that, despite the observed loss of reduced Fe escaping from modern hydrothermal vents and during plume dispersal through rapid chemical reactions with oxygenated seawater, the loss of Fe is much slower than previously thought (see Cartman and Findlay, 2020, for a review). The stabilization of Fe through binding with organic matter, inorganic nanoparticles, organic and inorganic colloids results in Fe being transported thousands of kilometers across the open modern ocean (Bennett et al., 2008; Toner et al., 2009; Sarder and Koschinsky, 20011; Yücel et al., 2011; Resing et al., 2015; Fitzsimmons et al., 2017; Lough et al., 2019). However, the higher mobility of Fe in the predominantly anoxic Precambrian seawater would have allowed for more stable transportation of Fe across oceans and for thorough mixing with seawater. Because shallow oxygenation of the surface ocean was prevalent at this time, contact with oxic marginal seawater would have promoted the precipitation and burial of hydrous ferric oxyhydroxides and their diagenetic products in the affected shallow water sediments. Fe concentrations of up to  $10^5$  ppm are recorded in the continental platform sediments in the Wanimzi Formation (Table 2), being about a factor of two greater than the concentrations in modern submarine hydrothermal systems (Tivey, 2007; German and Seyfried, 2014).

The variation in Fe and quartz content in the Fe-rich lithologies point to related changes in the intensity of the delivery of Fe-rich fluids to seawater (see for example Chi Fru et al., 2013; 2018). For instance, Zn/Co ratios with high and low values associated with hydrothermal and detrital influence, respectively (Toth, 1980; Halverson et al., 2011), largely decreased from the carbonates through to the overlying Neoproterozoic siliciclastic stromatolitic succession (Fig. 6f). Mo/W ratios, a measure of sediment formation from sulfide-rich fluids due to the high reactivity of Mo towards sulfide relative to W, are generally low (Fig. 6g). This observation suggests potential precipitation of particle-reactive thiomolybdate with sulfide minerals near the source of the Fe-rich fluids and subsequent precipitation of W enriched in the migrating plume relative to Mo with primary ferric Fe minerals on the oxygenated continental margin (see for example Mohajerinejad et al., 2016; Bauer et al., 2017; Dellwig et al., 2019).

The higher enrichment of W in the Fe-rich facies relative to the upper continental crust, the siliciclastic stromatolitic, and Taghdout carbonate rocks, support a significant supply of W to the basin by hydrothermal activity (Table 2). Consistent with the latter observation, the Fe-rich samples are ~2 and 4 times more enriched in W than the siliciclastic stromatolite-containing and carbonate facies, respectively (Table 2). Similarly, the strong enrichment of As and Sb in Fe-rich layers relative to the siliciclastic layer, the carbonates and upper continental crust are similar to those for Fe, consistent with a suggested hydrothermal origin of these elements (e.g., Breuer and Pichler, 2013; Feely et al., 1991; 1998, Chi Fru et al., 2013; Zeng et al., 2018; Table 2). The latter proposition is supported by a clear lack of similar significant enrichment of As, Sb, and Fe in the siliciclastic and carbonate layers relative to the upper continental crust. (Table 2). Th/U ratios frequently used as a redox proxy whereby U is enriched in deoxygenated sediments relative to Th (Kerrick et al., 2013; Manikyamba, 2018), are relatively low in the Fe-rich sequences compared to the reference overlying and underlying Fe-poor samples (Fig. 6h).

The above observations suggest intense and prolonged hydrothermal activity linked to an Fe-rich source that enabled significant Fe enrichment in the fluids that deposited the Wanimzi ironstones on the coast of the WAC.

The Fe concentrations were probably much higher in the pristine hydrothermal fluids emerging from the vents, given that substantial quantities of Fe would have been precipitated with hydrothermal sulfides near the vents as commonly observed at various modern hydrothermal vent fields. Combined, the Fe-rich fluids that formed the Wanimzi ironstones and the sharp absence of ironstones in the underlying and overlying successions suggest sudden initiation and termination of the supply of Fe-rich fluids to the WAC during deposition of the unique Wanimzi ironstones. Intriguingly, this proposition is consistent with the suggested age of the Wanimzi Formation being coincident with the inception of rifting and breakup of the Rodinia supercontinent dated at 920-890 Ma in many Proterozoic cratons (e.g. Evans et al., 2016; Zhou et al., 2018; Baratoux et al., 2019; Chavez et al., 2019) and in the Anti-Atlas at 883 Ma (Bouougri et al., 2020). Such widespread rifting event and supercontinent breakup would have inevitably led to the development of active submarine hydrothermal vent complexes.

In addition to Fe, prominent hydrothermal metals like Co, As, V, Sb, Pb and Cu (Tivey, 2007; Beuer and Pichler, 2013; German and Seyfried, 2014; Rouxel et al., 2018), show variable but stronger enrichments in the Wanimzi ironstones compared to the Fe-poor reference sequences (Fig. 6; Table 2). For instance, the concentration of As in the ironstones is up to 80 times greater than the 3000 times As concentrations discharged by some modern back and Island arc basin shallow submarine hydrothermal fluids compared to unadulterated seawater levels (e.g., Breuer and Pichler, 2013). Importantly, Fe-hematite sedimentary rocks deposited from these pristine high As-containing submarine As-rich hydrothermal fluids are reported to record similar anomalously high As concentrations (e.g., Chi Fru et al., 2013). Even more interestingly, the As concentrations in the Fe-rich lithologies are up to 1400 times in excess of concentrations in hydrothermal fluids from the East Pacific Rise and 4600 times over the values reported for the Mid-Atlantic Ocean Ridge (Breuer and Pichler, 2013). Further, the average As concentration in the Fe-rich lithologies is 18 and 9 times above those present in the overlying siliciclastic and underlying carbonates in the Taghdout Formation, respectively. This observation is most parsimoniously interpreted to represent the levels of As concentrations in the waters that formed the

different successions based on the assumption that the Fe content of the sediments did not skew the data towards the enrichment of As by the ferric Fe in the Wanimzi Formation. This appears not to have been the case considering that the As/Fe ratios in these sediments are generally homogenous across the entire succession (Appendix O). Moreover, the comparable behaviors of As and Sb (Fig. 6a-b) across the studied successions have previously been related to water mass type and interaction with rocks by hydrothermal fluids and migrating hydrothermal plumes emitted by active vents (Wu et al., 2017; Zeng et al., 2018). Importantly, 63 % of the As in the Fe-rich lithologies is explained by a positive covariance with Fe (Fig. 12a), similar to observations between hydrothermal ferric Fe and As (e.g., Feely et al., 1991; Chi Fru et al., 2015). Similar to the behavior of hydrothermal ferric Fe and V, a positive correlation was observed between V and Fe in the ironstones (Fig. 12b; Feely et al., 1998). Only a weak positive correlation was observed for Fe, Cu, and none for Mo. As and Mo showed a strong positive correlation (Fig. 12c), suggesting they likely had the same hydrothermal source considering that both can be strongly enriched in hydrothermal fluids (German and Seyfried, 2014). However, the lack of correlation between Fe and Mo implies that precipitation of Mo into the ironstones may have been independent of ferric Fe precipitation.

The As data suggest that the microbial communities associated with the water mass that formed the Fe-rich lithologies would have had to combat the dramatic effects of arsenic toxicity, which include inhibiting the synthesis and function of proteins by As(III) in reducing environments and cell phosphate uptake and metabolism by As(V) in oxygenated habitats (Cervantes et al., 1994; Smedley and Kinniburgh, 2002). Such a scenario would have impeded primary production, as is common in modern oceans, compared to the reference arsenic-poor settings. This would have had major implications for carbon fixation, organic carbon burial, and oxygenation by the activities of the marine cyanobacteria (Dyhrman and Haley, 2011; Wurl et al., 2013; Saunders and Rocap, 2016; Giovannoni et al., 2019). However, a full set of arsenic detoxifying genes believed to have been present by the earliest Tonian Period (Chen et al., 2020), together with widespread mechanisms for controlling genes that select for phosphate at the expense of As(V), would have

alleviated this situation to some extent. These genes have been shown to be abundant in a modern submarine hydrothermal system exposed to hydrothermal fluids containing 3000 times more As than seawater concentrations (Chi Fru et al., 2018b). This would have partially mitigated As toxicity when the deep-sea deoxygenated hydrothermal As-rich fluids rose and mixed with the shallow seawater on the coast of the WAC, possibly supporting asenotrophic microbial activity in the deoxygenated waters (Visscher et al., 2020). Similarly, key nutrients like Mo and V, critical for nitrogen fixation and thus primary production in the early oceans (Zhang et al., 2014), would have equally contributed to maintaining a good degree of primary production as reflected by the photosynthetic  $\delta^{13}\text{C}_{\text{org}}$  proxy signature preserved in the ironstones.

### 5.2.3. Insights from Fe isotope systematics

The  $\delta^{56}\text{Fe}$  values of modern sulfide-rich hydrothermal fluids at seafloor mid-ocean ridges typically range from  $-1.23\text{‰}$  to  $-0.14\text{‰}$  with a reported average of  $-0.52\text{‰}$  (Sharma et al., 2001; Severmann et al., 2004; Bennett et al., 2009; Li et al., 2017; Rouxel et al., 2016). These  $\delta^{56}\text{Fe}$ -depleted values are balanced by enriched seawater  $\delta^{56}\text{Fe}$  ratios that vary from  $-0.64\text{‰}$  to up to  $0.80\text{‰}$  with an estimated average of  $0.34\text{‰}$  (Bennet et al., 2009; Rouxel et al., 2016; Fitzsimmons et al., 2016, 2017; Karl et al., 2016; Li et al., 2017; Lough et al., 2017). In contrast, a mean value of  $+0.1\text{‰}$  has been suggested for sulfide-depleted hydrothermal fluids from Pele's pit in the Hawaiian Loihi submarine volcanic hotspot similar to neighboring seafloor basaltic  $\delta^{56}\text{Fe}$  ratios (Rouxel et al., 2018). The  $\delta^{56}\text{Fe}$  values are commonly controlled by a combination of biological and abiological processes, including chemical precipitation of Fe oxides during abiotic and biotic oxidation of Fe with oxygen, anoxic precipitation of Fe sulfide, microbial reduction of Fe, water rock interactions, and phase separation (e.g., Rouxel et al., 2008; Severmann et al., 2004; Li et al., 2017; Rouxel et al., 2018; Heard and Dauphas, 2020). However, there is a consensus that net seawater  $\delta^{56}\text{Fe}$  values are generally heavier relative to submarine hydrothermal fluids (Radic et al., 2011; Conway et al., 2014, 2015). For instance, high temperature hydrothermal fluids with light  $\delta^{56}\text{Fe}$  ratios of  $-0.23\text{‰}$  from the Rainbow hydrothermal vents precipitate

and deliver Fe with  $\delta^{56}\text{Fe}$  values similar to those recorded in the receiving deep North Atlantic seafloor sediments (e.g., Severmann et al., 2004). Further, studies have shown that Fe isotopes are more sensitive to local environmental conditions (e.g., precipitating authigenic sulfide and Fe oxyhydroxide minerals) than to extant biological and abiological processes (Lough et al., 2017; Rouxel et al., 2018). This implies that Fe isotopes are best applied as tracers of environmental change processes. The source and sink of Fe in the ocean and global Fe biogeochemical cycling are dependent on our knowledge of fluxes between various Fe pools and their associated isotopic signatures. Therefore, quantitative precipitation of primary Fe from seawater and hydrothermal fluids is expected to conservatively display  $\delta^{56}\text{Fe}$  values reflecting sources and variable mixing with seawater. Similarly, examining the behavior of Fe isotopes during the dispersal and transportation of hydrothermal plumes through seawater can provide information on the sources and sinks of Fe to seawater as well as the influence of hydrothermal Fe in the deposition of Fe Formations on ancient continental margins.

The variability of  $\delta^{56}\text{Fe}$  in the Fe-rich sedimentary units from the Wanimzi Formation are more similar to the signatures of hydrothermal fluids than for modern oxic seawater values that are often more homogeneously heavy. This view is supported by the transition from light to exceptionally heavy  $\delta^{56}\text{Fe}$  values in the overlying reference Fe-poor stromatolitic succession shown to have the least hydrothermal influence by their REE+Y and trace metal composition. Because Fe is insoluble in oxygenated seawater, its concentration in the modern ocean is usually in the nM to pM range, while  $\mu\text{M}$  to mM concentrations are documented in anoxic hydrothermal fluids and plumes (Elderfield and Schultz, 1996; Bennett et al., 2008; Fitzsimmons et al., 2014; Resing et al., 2015; Lough et al., 2017). Similar to this observation, the Fe-rich lithologies, which were deposited beneath anoxic bottom waters, are 26 times more enriched in Fe than the stromatolitic rocks, which we argue formed in full bottom water oxygenated conditions. Moreover, these Fe-rich lithologies contain  $\delta^{56}\text{Fe}$  signatures that on average are light (-0.03‰) compared to the heavy values of up 0.52‰ measured in the stromatolitic Fe-poor reference rocks that are believed to have experienced the least hydrothermal influence of all the samples. Further,

mid-ocean ridge plumes from the East Pacific Rise with similar  $\delta^{56}\text{Fe}$  values of  $-0.91\text{‰}$  and  $-0.03\text{‰}$  were interpreted to have resulted from variable mixing of hydrothermal fluids with seawater, lithospheric interactions, and biogenic Fe cycling (Rouxel et al., 2016).

The lowest  $\delta^{56}\text{Fe}$  value of  $-0.41\text{‰}$  in the Wanimzi ironstones has been reported for Fe particles in endmember hydrothermal plumes following systematic stripping of light  $^{56}\text{Fe}$  by Fe sulfide minerals (Rouxel et al., 2016). In the absence of direct evidence for the sulfide content of the original fluids that formed the ironstones, Mo/W ratios are used as proxies for Mo depletion and W enrichment during the precipitation of particulate sulfide minerals (Mohajarin et al., 2016; Bauer et al., 2017; Delwig et al., 2019). Upon transition to conditions that support the production of ferric Fe, W is preferentially sequestered relative to Mo. The variable levels of Mo/W ratios in the Fe-rich lithologies (Fig. 6g) may therefore be linked to the influence of sulfide fluids. However, owing to the absence of correlation amongst Mo, W and Fe, it is suggested that Mo and W enrichments in the ironstones were not the direct results of Fe precipitation. The positive correlation between Mo and As in the Fe-enriched lithologies (Fig. 12c), both being strong chalcophiles possessing high affinities for sulfide, suggests low sulfide concentration in the source vent fluids. This, allowed substantial amounts of As, Mo, and Fe to escape precipitation with vent sulfides and subsequent enrichments in the ironstones. The mainly heavier  $\delta^{56}\text{Fe}$  signal of up to  $+0.61\text{‰}$  recorded in the Fe-poor siliciclastic Mn-Ti reference rocks and their REE+Y distribution, are comparable to values recorded in some modern seawater. In addition, these reference Fe-poor rocks lack evidence for strong hydrothermal influence, while the lighter  $\delta^{56}\text{Fe}$  values in the ironstones are more consistent with a hydrothermal source.

Our  $\delta^{56}\text{Fe}$  values fall within the range for published Proterozoic Fe formations believed to have been influenced by varying degrees of hydrothermal input (Planavsky et al., 2010; Yan et al., 2010; Halverson et al., 2011; Li et al., 2017; Heard and Dauphas, 2020; Fig. 11b). The simple hematite and quartz mineralogy of the Wanimzi ironstones is comparable to the reported predominance of hematite in syn-glacial Neoproterozoic Snowball Fe formations (Bekker et al., 2010; Halverson et al., 2011; Cox et

al., 2013; Lechte et al., 2013). However, the narrower range of  $\delta^{56}\text{Fe}$  values in the Wanimzi ironstones (-0.41‰ to 0.35‰) are more similar to modern hydrothermal  $\delta^{56}\text{Fe}$  seafloor deposits (Planavsky et al., 2010; Rouxel et al., 2008; 2016; 2018), while the wider range in  $\delta^{56}\text{Fe}$  values of -0.7‰ to 1.2‰ in Neoproterozoic syn-glacial Fe formations compared to the narrower records in the Wanimzi Fe-rich lithologies, point perhaps to varying degrees of partial Fe oxidation (e.g., Halverson et al., 2011; Table 3).

The data suggest that the relationship between Fe concentrations and Zn/Co ratios may be a stronger indicator of the degree of hydrothermal influence than the relationship between  $\delta^{56}\text{Fe}$  and Zn/Co ratios in the studied succession. For instance, although  $\delta^{56}\text{Fe}$  lacked a significant negative correlation with Fe concentrations and the Zn/Co ratios, a goodness of fit positive correlation between Fe and Zn/Co points to hydrothermal activity contributing to at least 64 % of bulk Fe enriched in the Fe-rich sediments (Appendix P). Further, while Fe concentrations in the Wanimzi Formation are much elevated relative to the underlying Paleoproterozoic Taghdout carbonates and the overlying Ediacaran Imi n-Tizi siliciclastic deposits, the Zn/Co ratios of the Wanimzi ironstones are lower compared to the Fe-poor carbonates and higher relative to the Fe-poor Ediacaran deposit. This suggests potential mixing of seawater with Fe-poor hydrothermal fluids during the deposition of the Taghdout carbonates and progressively negligible hydrothermal influence during the deposition of the siliciclastic rocks above the Wanimzi ironstones. The positive  $\delta^{56}\text{Fe}$  values of the Fe-poor, non-hydrothermal siliciclastic sediments above the Wanimzi ironstones, linked to low seawater Fe concentration and Zn/Co ratios, reflect expected heavier  $\delta^{56}\text{Fe}$  values resulting from low seawater Fe concentration and hydrothermal activity in some modern seawater settings. Moreover, quantitative and partial oxidation of Fe by biotic and abiotic processes, would result in quantitative or partial fractionation of Fe isotopes between the precipitated Fe(III) and residual dissolved hydrothermal Fe(II), decoupling the  $\delta^{56}\text{Fe}$  and Zn/Co signals.

### 5.3. Redox depositional conditions

The pronounced  $Ce_{SN}$  depletion observed in our samples is a feature common to modern oxygenated seawater (e.g., Bau and Dulski, 1996; Singh and Rajamani, 2001; Shields et al., 2004; Bau and Koschinsky, 2009). Statistical test for the redox state of seawater by the calculated true negative  $Ce/Ce^*$  anomaly, indicates extensive oxygenation of the WAC margin (Fig. 10a; Bau, 1996; Planavsky et al., 2010). However, redox reconstruction using the Fe-based redox proxy (Poulton and Canfield, 2005; Poulton and Canfield, 2011; Clarkson et al., 2014) suggests deposition of both the reference siliciclastic carbonates from the Taghdout Formation and the Wanimzi ironstone lithologies occurred beneath a deoxygenated water column, while full water column oxygenation coincides with the reference Fe-poor siliciclastic Imi n'Tizi rocks. Persistent ferruginous conditions were widespread at this time while euxinia is not supported by the data.

The siliciclastic detritus derived from continental weathering likely influenced the REE+Y distribution patterns, as supported by the corresponding average Y/Ho clastic values. Importantly, because the entire sequence is siliciclastic, the divergent redox conditions indicated by the  $Ce/Ce^*$  and the Fe-based redox proxies, are interpreted to reflect the unique ability of the Fe-based redox proxy to record the emergent anoxic bottom water depositional conditions induced by the fluids that delivered Fe to the continental margin. Further, as the chemocline deepens, the Y/Ho ratios are expected to decrease as the  $Ce/Ce^*$  anomaly increases because of effective dissolution of  $Fe(II)(ox/hydr)oxide$  particles that tend to be relatively enriched in Ho and Ce (Bau et al., 1997; Planavsky et al., 2010; Halverson et al., 2011). Instead the lack of an inverse correlation between Y/Ho and  $Ce/Ce^*$ , together with static average Y/Ho ratios across the sampled section, are consistent with a stable shallow marine platform experiencing little or no change in the depth of the chemocline.

We propose that the shallow margins of the WAC were fully oxygenated prior to the process that introduced Fe-rich fluids to the platform waters. This suggestion implies that the process that conveyed the ferruginous fluids to the WAC margin to promote kinetic deoxygenation of the shallow seawater mass was too rapid to allow equilibration with the atmosphere and the establishment of a stable chemocline with fluctuating depth. Moreover, the

Y/Ho ratios being more similar to composite shale and clastic sediment values, imply that the REE+Y values are influenced by contribution of clast weathered from the upper continental crust, relative to hydrothermal input. This is consistent with the lack of meaningful correlation between the inferred hydrothermal Fe and corresponding Y/Ho ratios, a strong seawater Ce<sub>SN</sub> and subtle Eu<sub>SN</sub> anomalies, the latter being undetectable in some cases. The negative  $\delta^{57}\text{Fe}$  correlation to Y/Ho ratios recorded in syn-glacial Neoproterozoic Fe formations isolated from continental contamination by detrital material, and marked by the scavenging of REE+Y by Fe oxides precipitated from a deepening chemocline (Halverson et al., 2011), is not observed in our samples.

Instead, the Fe-based redox proxy points to a sudden deoxygenation event of what was likely a fully oxygenated shallow water mass by anoxic submarine hydrothermal plumes released from a distal anoxic deep-sea source. Attenuation of the REE+Y hydrothermal signal is interpreted to be the product of long distance plume transportation to the continental margin. As a result, vigorous mixing of the migrating plume with seawater and particle precipitation, systematically weakened the hydrothermal REE+Y signal (Fig. 13). This observation is supported by the attenuated hydrothermal Eu signature, reported for various Precambrian IFs to be related to high temperature hydrothermal provenance of Fe (Michard, 1989; Klein and Beukes, 1993; Halverson et al., 2011).

The Fe-based redox trends are supported by variations in associated redox sensitive trace metals such as elevated levels of U and V in the Fe-rich lithologies (Fig. 6-c; Table 2). For example, U concentrations average  $1.6 \pm 0.6$  ppm in the ironstones compared to  $1.0 \pm 0.5$  ppm and  $\sim 0.4 \pm 0.0$  ppm in the reference Fe-poor siliciclastic rocks above and beneath the Fe-rich sequence, respectively. Similarly, V concentrations averaged  $70.8 \pm 50.6$  relative to  $36.3 \pm 6.6$  ppm and  $\sim 8.5$  for the Fe-poor rocks above and below the Fe-rich layer, respectively. These average values are below continental crust concentrations of 2.8 ppm and 107 ppm for U and V, respectively (McLennan (2001). Nonetheless, the higher co-enrichment of U and V in the Fe-rich lithologies relative to the Fe-poor lithologies, is consistent with the strong anoxic, non-euxinic, ferruginous depositional conditions established by our Fe

speciation analysis in Figure 10b-c (e.g., Tribovillard et al., 2006; Scott et al., 2008; Scott & Lyons, 2012). Equally, the lack of any meaningful Mo enrichment is consistent with the absence of euxinic conditions suggested by our Fe speciation data across the studied section (Fig. 6a).

## 6. Conclusions

We present a siliciclastic ironstone deposit estimated to be of Early Neoproterozoic age in the Anti Atlas Mountains of Morocco, marked by a unique hematite enrichment style different from that reported for most Precambrian Fe Formations. The data indicate a predominantly anoxic deep ocean that enabled the transportation and delivery of strongly reducing submarine hydrothermal plumes to an oxygenated early Neoproterozoic shallow marine wave-influenced platform. Here, reduced Fe was mixed with and oxidized by oxygenated seawater and deposited in association with siliciclastic material weathered from the continent. Based on the combined Ce/Ce\* anomaly and Fe-based bottom water redox reconstruction, we propose that the marginal shallow seawaters were fully oxygenated until the anoxic hydrothermal fluids upwelled from the deep-sea and rapidly deoxygenated the shallow waters for an extended period of time. This resulted in the oxidation of upwelling reduced hydrothermal ferrous Fe and the deposition of primary ferric Fe that was preserved as hematite in the Wanimzi ironstones. The data further suggest that, in addition to the open oceans being redox stratified to enable large-scale migration of reduced hydrothermal plumes to the WAC margin, the breakup of Rodinia supercontinent may have initiated widespread early Neoproterozoic redox processes that orchestrated extended episodes of widespread shallow seawater anoxia in affected basins. This observation is consistent with the proposition that increased deposition of ferric Fe during the Early Neoproterozoic may have suppressed extensive seawater-atmosphere oxygenation through the scavenging and burial of dissolved phosphate by ferric Fe particles precipitating from seawater (Guilbard et al., 2020).

## Acknowledgements

This work was funded by the European Research Council (Grant No. 336092 to ECF). We acknowledge funding support from Hassan II Academy of Science and Technology (HIIAST/SDU/2016.02 El Albani et al.) and the funding fellowship awarded to I. Chraiki).

### Declaration of interests

The authors declare that they have no known competing financial interests or personal relationships that could have appeared to influence the work reported in this paper.

### References

- Baratoux, L., Söderlund, U., Ernst, R.E., de Roever, E., Jessell, M.W., Kamo, S., Naba, S., Perrouty, S., Metelka, V., Yate, L., Grenholm, M., Diallo, D.P., Ndiaye, P.M., Dioh, E., Cournède, C., Benoit, M., Baratoux, D., Youbi, N., Rousse, S., Bendaoud, A., 2019. New U–Pb Baddeleyite ages of mafic dyke swarms of the West African and Amazonian Cratons: implication for their configuration in supercontinents through time. In: Srivastava, R.J., Ernst, R.E., Peng, P (Eds.), *Dyke Swarms of the World: A Modern Perspective*, Springer, Singapore, pp. 263–314.
- Bau, M., Dulski, P. (1996). Distribution of yttrium and rare-earth elements in the Penge and Kurur iron-formations, Transvaal Supergroup, South Africa. *Pre. Res.* 79:37–55. [https://doi.org/10.1016/0301-9268\(95\)00087-9](https://doi.org/10.1016/0301-9268(95)00087-9).
- Bau, M., Mdlar, F., Dulski, P., 1997. Yttrium and lanthanides in eastern Mediterranean seawater and their fractionation during redox-cycling. *Mar. Chem.* 56:123–131. [https://doi.org/10.1016/S0304-4203\(96\)00091-6](https://doi.org/10.1016/S0304-4203(96)00091-6).
- Bau, M., Dulski, P., 1999. Comparing yttrium and rare earths in hydrothermal fluids from the Mid-Atlantic Ridge: implications for Y and REE behaviour during near-vent mixing and for the Y/Ho ratio of Proterozoic seawater. *Chem. Geol.* 155:77–90. [https://doi.org/10.1016/S0009-2541\(98\)00142-9](https://doi.org/10.1016/S0009-2541(98)00142-9).
- Bau, M., Koschinsky, A., 2009. Oxidative scavenging of cerium on hydrous Fe oxide: Evidence from the distribution of rare earth elements and yttrium between Fe oxides and Mn oxides in hydrogenetic ferromanganese crusts. *Geochem. J.* 43:37–47. <https://doi.org/10.2343/geochemj.1.0005>.
- Bauer, S., Blomqvist, S., Ingri, J., 2017. Distribution of dissolved and

- suspended particulate molybdenum, vanadium, and tungsten in the Baltic Sea. *Mar. Chem.* 196:135–147. <https://doi.org/10.1016/j.marchem.2017.08.010>.
- Bekker, A., Slack, J.F., Planavsky, N., Krapež, B., Hofmann, A., Konhauser, K.O., Rouxel, O.J., 2010. Iron Formation: The Sedimentary Product of a Complex Interplay among Mantle, Tectonic, Oceanic, and Biospheric Processes. *Econ. Geol.* 105:467–508. <https://doi.org/10.2113/econgeo.107.2.379>.
- Bennett, S.A., Achterberg E.P., Connelly, D.P., Statham, P.J., Fones, G.R., German, I.C.R., 2008. The distribution and stabilisation of dissolved Fe in deep-sea hydrothermal plumes. *Earth Planet. Sci. Letts.* 270:157–167. <https://doi.org/10.1016/j.epsl.2008.01.048>.
- Bennett, S.A., Rouxel, O., Schmidt, K., Garbe-Schönberg, D., Statham, P.J., German, C.R., 2009. Iron isotope fractionation in a buoyant hydrothermal plume, 5°S Mid-Atlantic Ridge. *Geochim. Cosmochim. Acta* 73:5619–5634. <https://doi.org/10.1016/j.gca.2009.06.027>.
- Bouougri, E. H., Ait Lahna, A., Tessinari, C. C. G., Basei, M. A. S., Youbi, N., Admou, H., Saquaque, A., Boumehdi, A., Maacha, L., 2020. Time constraints on Early Tertiary Rifting and Cryogenian Arc terrane-continent convergence along the northern margin of the West African craton: Insights from SHRIMP and LA-ICP-MS zircon geochronology in the Pan-African Anti-Atlas belt (Morocco). *Gond. Res.* 85:169–188. <https://doi.org/10.1016/j.gr.2020.03.011>.
- Bouougri, E. H. and Porada, H., 2011. Biolaminated siliciclastic deposits. In: *Advances in Stromatolite Geobiology, Lecture Notes in Earth Sciences*, Springer Switzerland, pp. 507–524.
- Bouougri, E. H. and Saquaque, A., 2004. Lithostratigraphic framework and correlation of the Neoproterozoic northern West African Craton passive margin sequence (Siroua-Zenaga-Bouazzar Elgraara Inliers, Central Anti-Atlas, Morocco): An integrated approach. *J. Afri. Earth Sci.* 39:227–238. <https://doi.org/10.1016/j.jafrearsci.2004.07.045>.
- Bouougri, E., 2003. The Moroccan Anti-Atlas: the West African craton passive margin with limited Pan-African activity. Implications for the northern limit of the craton – discussion. *Pre. Res.* 120:179–183.

- [https://doi.org/10.1016/S0301-9268\(02\)00169-9](https://doi.org/10.1016/S0301-9268(02)00169-9).
- Bouougri, E. and Porada, H., 2002. Mat-related sedimentary structures in Neoproterozoic peritidal passive margin deposits of the West African Craton (Anti-Atlas, Morocco). *Sed. Geol.* 153:85–106. [https://doi.org/10.1016/S0037-0738\(02\)00103-3](https://doi.org/10.1016/S0037-0738(02)00103-3).
- Bouougri, E. H. and Saquaque, A., 2000. Organisation stratigraphique et structure de la marge Anti-Atlasique du craton Ouest-Africain au sud du Siroua (Néoprotérozoïque, Anti-Atlas central, Maroc). *Comptes Rendus de l'Académie Des Sciences - Series IIA - Earth Planet. Sci.* 330:753–759. [https://doi.org/10.1016/S1251-8050\(00\)00232-9](https://doi.org/10.1016/S1251-8050(00)00232-9).
- Breuer, C., Pichler T., 2013. Arsenic in marine hydrothermal fluids. *Chem. Geol.* 348:2–14. <https://doi.org/10.1016/j.chemgeo.2012.10.044>.
- Brocks, J. J., Jarett, A.J.M., Sirantoine, E., Halmann, C., Hoshino, Y, and Liyanage T., 2017. The rise of algae in Cryogenian oceans and the emergence of animals. *Nature* 548:573–581. DOI:10.1038/nature23457.
- Canfield, D. E., 1998. A new model for Proterozoic ocean chemistry. *Nature* 396:450–453. DOI:10.1038/24859.
- Cervantes, C., Ji, Guangyong, Ramirez, J.L., Silver, S., 1994. Resistance to arsenic compounds in microorganisms. *FEMS Microbiol. Rev.* 15:355–367. [https://doi.org/10.1016/0168-6445\(94\)90069-8](https://doi.org/10.1016/0168-6445(94)90069-8).
- Chavez, A.D.O., Ernst, R.E., Söderlund, U., Wang, X., Naeraa, T., 2019. The 920–900 Ma Bahia-Gangila lip of the São Francisco and Congo cratons and link with Dashigou-Chulan lip of North China craton: new insights from U-Pb geochronology and geochemistry. *Pre. Res.* 329, 124–137. <https://doi.org/10.1016/j.precamres.2018.08.023>.
- Chen, S.-C., Suna, G.-X., Yan, Y., Konstantinidis, K.T., Zhange, S.-Y., Deng, Y., Lia, X.-M., Cuia, H.-L., Musat, F., Popp, D., Rosenh, B.P., Y.-G., Zhu., 2020. The Great Oxidation Event expanded the genetic repertoire of arsenic metabolism and cycling. *Proc. Natl. Sci. U.S.A.* 117:10414–10421. <https://doi.org/10.1073/pnas.2001063117>.
- Chi Fru, E., Piccinelli, P, Fortin, D., 2012. Insights into the global microbial community structure associated with iron oxyhydroxide minerals deposited in the aerobic biogeosphere. *Geomicrobiol. J.* 29:587–610. <https://doi.org/10.1080/01490451.2011.599474>.

- Chi Fru, E., Ivarsson, M., Kiliyas, S.P., Bengtson, S., Belivanova, V., Marone, F., Fortin, D., Broman, C., Stampanoni, M., 2013. Fossilized iron bacteria reveal a pathway to the biological origin of banded iron formation. *Nature Comms* 4:2050. DOI: 10.1038/ncomms3050.
- Chi Fru, E., Arvestål, E., Callac, N., El Albani, A., Kiliyas, S., Argyraki, A., and Jakobsson, M., 2015a. Arsenic stress after the Proterozoic glaciations. *Sci. Rep.* 5:17789. DOI: 10.1038/srep17789.
- Chi Fru, E., Ivarsson, M., Kiliyas, S.P., Frings, P.J., Hemmingsson, C., Broman, C., Bengtson, S., Chatzitheodoridis, E., 2015b. Biogenicity of an Early Quaternary iron formation, Milos Island, Greece. *Geobiology* 13:225-244. <https://doi.org/10.1111/gbi.12128>.
- Chi Fru, E., Rodríguez, N.P., Partin, C.A., Lalonde, S.V., Andersson, P., Weiss, D.J., El Albani, A., Rodushkin, I., and Konhauser, K.O., 2016a. Cu isotopes in marine black shales record the Great Oxidation Event. *Proc. Natl. Acad. Sci. U.S.A.* 113:4941–4946. <https://doi.org/10.1073/pnas.1523544113>.
- Chi Fru, E., Hemmingsson, C., Helm, M., Chiu, B., Iñiguez E., 2016b. Arsenic-induced phosphate limitation under experimental Early Proterozoic oceanic conditions. *Earth Planet. Sci. Letts.* 434:52–63. <https://doi.org/10.1016/j.epsl.2015.11.009>.
- Chi Fru, E., Kiliyas, S., Ivarsson, M., Rattray, J.E., Gkika, K., McDonald, I., He, Q., Broman, C., 2018a. Sedimentary mechanisms of a modern banded iron formation on Milos Island, Greece. *Solid Earth* 9:573–598. <https://doi.org/10.5194/se-9-573-2018>.
- Chi Fru, F., Callac, N., Posth, N.R., Argyraki, A., Ling, Y.-C., Ivarsson, M., Broman, C., Kiliyas, S.P., 2018b. Arsenic and high affinity phosphate uptake gene distribution in shallow submarine hydrothermal sediments. *Biogeochemistry* 141:41–62. <https://doi.org/10.1007/s10533-018-0500-8>.
- Chi Fru, E., Somogyi, A., El Albani, A., Medjoubi, K., Aubineau, J., Robbins, L.J., Lalonde, S.V., and Konhauser, K.O., 2019. The rise of oxygen-driven arsenic cycling at ca. 2.48 Ga. *Geology* 47:243–246. <https://doi.org/10.1130/G45676.1>.
- Choubert, G., 1947. L'accident majeur de l'Anti-Atlas, C.R. Acad. Sci. Paris, 224:1172–1173.

- Clarkson, M.O., Poulton, S.W., Guilbaud, R., Wood, R.A., 2014. Assessing the utility of the Fe/Al and Fe-speciation to record water column redox conditions in carbonate-rich sediments. *Chem. Geol.* 382:111–122. <https://doi.org/10.1016/j.chemgeo.2014.05.031>.
- Conway, T.M., John, S.G., 2014. Quantification of dissolved iron sources to the North Atlantic ocean. *Nature* 511:212–215. DOI:10.1038/nature12382.
- Conway, T.M., John, S.G., 2015. The cycling of iron, zinc and cadmium in the North East Pacific Ocean-Insights from stable isotopes. *Geochim. Cosmo. Acta* 164:262–283. <https://doi.org/10.1016/j.gca.2015.05.023>.
- Cox, G.M., Halverson, G.P., Minarik, W.G., Le Heron, D.P., Macdonald, F.A. Bellefroid, E.J. Strauss, J.V., 2013. Neoproterozoic iron formation: An evaluation of its temporal, environmental and tectonic significance. *Chem. Geol.* 362:232–249. <https://doi.org/10.1016/j.chemgeo.2013.08.002>.
- Craddock, P.R., Bach, W., Seewald, J.S., Rouxel, O.J. Reeves, E, Tivey, M.K., 2010. Rare earth element abundances in hydrothermal fluids from the Manus Basin, Papua New: indicators of sub-seafloor hydrothermal processes in backarc basins. *Geochim. Cosmochim. Acta* 74:675–683. <https://doi.org/10.1016/j.gca.2010.07.003>.
- Craddock, P.R., Dauphas, N., 2011. Iron and carbon isotope evidence for microbial iron respiration throughout the Archean. *Earth Planet. Sci. Letts.* 303:121–132. <https://doi.org/10.1016/j.epsl.2010.12.045>.
- Dauphas, N., John, S.G., Rouxel, O., 2016. Iron isotope systematics. *Rev. Min. Geochem.* 82:415–510. <http://dx.doi.org/10.2138/rmg.2017.82.11>.
- Dellwig, O., Wegwerth, W., Schnetger, B., Schulz, H., Arz H.W., 2019. Dissimilar behaviors of the geochemical twins W and Mo in hypoxic-euxinic marine basins. *Earth-Sci. Rev.* 193:1–23. <https://doi.org/10.1016/j.earscirev.2019.03.017>.
- Douville E., Bienvenu P., Charlou J. L., Donval J. P., Fouquet Y., Appriou P. and Gamo T., 1999. Yttrium and rare earth elements in fluids from various deep-sea hydrothermal systems. *Geochim. Cosmochim. Acta* 63:627–643. [https://doi.org/10.1016/S0016-7037\(99\)00024-1](https://doi.org/10.1016/S0016-7037(99)00024-1).
- Douville, E., Charlou, J.L., Oelkers, E.H., Bienvenu, P., C.F. Colon, J., Donval,

- J.P., Fouquet, Y., Prieur, D., Appriou, P., 2002. The rainbow vent fluids (3614VN, MAR): the influence of ultramafic rocks and phase separation on trace metal content in Mid-Atlantic Ridge hydrothermal fluids. *Chem. Geol.* 184:37–48. [https://doi.org/10.1016/S0009-2541\(01\)00351-5](https://doi.org/10.1016/S0009-2541(01)00351-5).
- Dyhrman, S.T., Haley, S.T., 2011. Arsenate resistance in the unicellular marine Di <https://doi.org/10.3389/fmicb.2011.00214>.
- Dymek, R.F., Klein, C., 1988. Chemistry, petrology and origin of banded iron-formation lithologies from the 3800 MA isua supracrustal belt, West Greenland. *Pre. Res.* 39:247–302. [https://doi.org/10.1016/S0009-2541\(01\)00351-5](https://doi.org/10.1016/S0009-2541(01)00351-5).
- Elderfield H. and Schultz A., 1996. Mid-ocean ridge hydrothermal fluxes and the chemical composition of the ocean. *Annu. Rev. Earth Planet. Sci.* 24:191–224. <https://doi.org/10.1146/annurev.earth.24.1.191>.
- El Hadi, H., Simancas, J.F., Martinez-Poyatos, D., Azor, A., Tahiri, A., Montero, P., Fanning, C.M., Bea, F., Gonzalez-Lodeiro, F., 2010. Structural and geochronological constraints on the evolution of the Bou Azzer Neoproterozoic ophiolite (Anti-Atlas, Morocco). *Pre. Res.* 182:1–14. <https://doi.org/10.1016/j.precamres.2010.06.011>.
- Ennih, N., Liégeois, J.-P., 2001. The Moroccan Anti-Atlas: the West African craton passive margin with limited Pan-African activity. Implications for the northern limit of the craton. *Pre. Res.* 112:289–302. [https://doi.org/10.1016/S0301-9268\(01\)00195-4](https://doi.org/10.1016/S0301-9268(01)00195-4).
- Ennih, N., Liégeois, J.-P., 2008. The boundaries of the West African craton, with special reference to the basement of the Moroccan metacratonic Anti-Atlas belt. *Geological Society London, Special Publication* 297:1–17. <https://doi.org/10.1144/SP297.1>.
- Evans, D.A.D., Trindade, R.I.F., Catelani, E.L., D'Agrella-Filho, M.S., Heaman, L.M., Oliveira, E.P., Söderlund, U., Ernst, R.E., Smirnov, A.V., Salminen, J.M., 2016. Return to Rodinia? Moderate to high palaeolatitude of the São Francisco/Congo craton at 920 Ma. *Geological Society London, Special Publication* 424:167–190. <https://doi.org/10.1144/SP424.1>.
- Feely, R. A., Trefry, J. H., Lebon, G. T., German C. R., 1998. The relationship between P/Fe and V/Fe ratios in hydrothermal precipitates and dissolved

- phosphate in seawater. *Geophys. Res. Lett.* 15:2253–2256. <https://doi.org/10.1029/98GL01546>.
- Feely, R. A., Trefry, J. H., Massoth, G. J., Metz, S. A., 1991. Comparison of the scavenging of phosphorus and arsenic from seawater by hydrothermal iron oxyhydroxides in the Atlantic and Pacific Oceans. *Deep-Sea Res.* 38:617–623. [https://doi.org/10.1016/0198-0149\(91\)90001-V](https://doi.org/10.1016/0198-0149(91)90001-V).
- Fischer, W.W., Knoll, H.A., 2009. An iron shuttle for deepwater silica in Late Archean and early Paleoproterozoic iron formation. *GSA Bulletin*: 121:222–235. <https://doi.org/10.1130/B26328.1>.
- Fitzsimmons J. N., Boyle E.A., Jenkins W.J., 2014. Distal transport of dissolved hydrothermal iron in the deep South Pacific Ocean. *Proc. Natl. Acad. Sci. U.S.A.* 111:16654–16661. <https://doi.org/10.1073/pnas.1418778111>.
- Fitzsimmons J.N., Conway T.M., Lee J.M., Kayser R., Thyng K.M., John S. G., Boyle E.A., 2016. Dissolved iron and iron isotopes in the southeastern Pacific Ocean. *Glob. Biogeochem. Cycl.* 30:1372–1395. <https://doi.org/10.1002/2015GB005357>.
- Fitzsimmons J.N., John S.G., Marsay C.M., Hoffman C.L., Nicholas S.L., Toner B.M., German C.R. and Sherrell R.M., 2017. Iron persistence in a distal hydrothermal plume supported by dissolved-particulate exchange. *Nat. Geosci.* 10:U119–U150. <https://doi.org/10.1038/ngeo2900>.
- Frei, R., Dahl, P.S., Duke, E.F., Frei, K.M., Rintza, H., Frandsson, M.M., Jensen, L.A., 2008. Trace element and isotopic characterization of Neoproterozoic and Paleoproterozoic iron formations in the Black Hills (South Dakota, USA): Assessment of chemical change during 2.9-1.9 Ga deposition bracketing the 2.4-2.2 Ga first rise of atmospheric oxygen. *Pre. Res.* 162:441–474. <https://doi.org/10.1016/j.precamres.2007.10.005>.
- Gartman, A., Findlay, A.J., 2020. Impacts of hydrothermal plume processes on oceanic metal cycles and transport. *Nat. Geosci.* 13:396–402.
- German, C.R., and Seyfried, W.E., Jr., 2014. Hydrothermal processes. In *Treatise on Geochemistry*, 2nd edn. Oxford, Elsevier, Vol. 8, pp. 191–233.
- Giovannoni, S.J., Halsey, K.H., Saw, J., Muslin, O., Suffridge, C.P., Sun, J.,

- Lee, C.-P., Moore, E.R., Temperton, B., Noell, S.E., 2019. A parasitic arsenic cycle that shuttles energy from phytoplankton to heterotrophic bacterioplankton. *mBio* 10:e00246-19. doi:10.1128/mBio.00246-19.
- Guilbaud, R., Poulton, S.W., Thompson, J., Husband, K.F., Zhu, M., Zhou, Y., Shields, G.A., Lenton, T.M., 2020. Phosphorus-limited conditions in the early Neoproterozoic ocean maintained low levels of atmospheric oxygen. *Nat. Geosci.* 13:296–30. <https://doi.org/10.1038/s41561-020-0548-7>.
- Halverson, G.P., Poitrasson, F., Hoffman, P.F., Nédélec, A., Montel, J.-M., Kirby, J., 2011. Fe isotope and trace element geochemistry of the Neoproterozoic syn-glacial Rapitan iron formation. *Earth Planet. Sci. Letts.* 309:100–112. <https://doi.org/10.1016/j.epsl.2011.06.021>.
- Haugaard, R., Pecoits, E., Lalonde, S., Rouxel, C., Konhauser, K., 2016. The Joffre banded iron formation, Hamersley Group, Western Australia: Assessing the palaeoenvironment through detailed petrology and chemostratigraphy. *Precambrian Res.* 273:12–37. <https://doi.org/10.1016/j.precambres.2015.10.024>.
- Heard, A.W., Dauphas, N., 2020. Constraints on the coevolution of oxic and sulfidic ocean iron sinks from Archean–Paleoproterozoic iron isotope records. *Geology* 48:53–56. <https://doi.org/10.1130/G46951.1>.
- Heimann, A., Johnson, C.M., Beard, B.L., Valley, J.W., Roden, E.E., Spicuzza, M.J., Eukes, N.J., 2010. Fe, C, and O isotope compositions of banded iron formation carbonates demonstrate a major role for dissimilatory iron reduction in ~2.5 Ga marine environments. *Earth Planet. Sci. Letts.* 294:8–18. <https://doi.org/10.1016/j.epsl.2010.02.015>.
- Hemmingsson, C., Pitcairn, I.K., Chi Fru, C., 2018. Evaluation of phosphate-uptake mechanisms by Fe (III)(oxyhydr) oxides in Early Proterozoic oceanic conditions. *Environ. Chem.* 15:18–28. <https://doi.org/10.1071/EN17124>.
- Hoffman, P.F., Abbot, D.S., Ashkenazy, Y., Benn, D.I., Brocks, J., Coheren, P.A., Cox, G.M., Creveling, J.R., Erwin, D.H., Fairchild, I.J., Ferreira, D., Goodman, J.C., Halverson, G.P., Jansen, M.F., Fe Hir, G., Love, G.D., Macdonald, F.A., Maloof, A.C., Partin, A.C., Ramstein, G., Rose, B.E.J., Rose, C.V., Sadler, P.M., Tziperman, E., Voigt, A., Warren, S.G., 2017.

- Snowball Earth climate dynamics and Cryogenian geology-geobiology. *Sci. Adv.* 3:e1600983. DOI:10.1126/sciadv.1600983.
- Hefferan, K.P., Admou H., Karson, J.A., Saquaque, A., 2000. Anti-Atlas (Morocco) role in Neoproterozoic Western Gondwana reconstruction. *Pre. Res.* 103:89–96. [https://doi.org/10.1016/S0301-9268\(00\)00078-4](https://doi.org/10.1016/S0301-9268(00)00078-4).
- Inglis, J.D., D'Lemos, R.S., Samson, S.D., Admou, H., 2005. Geochronological constraints on Late Precambrian intrusion, metamorphism, and tectonism in the Anti-Atlas mountains. *The J. Geol.* 113:439–450. <https://doi.org/10.1086/430242>.
- Jessell, M.W., Begg, G.C., Miller, M.S., 2016. The geophysical signatures of the West African craton. *Prec. Res.* 274:3–24. <https://doi.org/10.1016/j.precamres.2015.08.010>.
- Kerrich, R., Said, N., Manikyamba, C., Wyman, D., 2013. Sampling oxygenated Archean hydrosphere: Implications from fractionations of Th/U and Ce/Ce\* in hydrothermally altered volcanic sequences. *Gond. Res.* 23:506–525. <https://doi.org/10.1016/j.gr.2012.02.007>.
- Keyser, W., Ciobanu, C.L., Cook, N.J., Johnson, G., Feltus, H., Johnson, S., Dmitrijeva, M., Ehrig, K., Nguyen, P.T., 2018. Petrography and trace element signatures of iron-oxides in deposits from the middleback Ranges, South Australia. From banded iron formation to ore. *Ore Geol. Rev.* 93:337–360. <https://doi.org/10.1016/j.oregeorev.2018.01.006>.
- Klein, C., Beukes, N.J., 1993. Sedimentology and geochemistry of the glaciogenic late Proterozoic Rapitan Iron-Formation in Canada. *Econ. Geol.* 88:542–565. <https://doi.org/10.2113/gsecongeo.88.3.542>.
- Klinkhammer, G.P., Elderfield, H., Edmond, J.M., Mitra, A., 1994. Geochemical implications of rare earth element patterns in hydrothermal fluids from mid-ocean ridges. *Geochim. Cosmochim. Acta* 58:5105–5113. [https://doi.org/10.1016/0016-7037\(94\)90297-6](https://doi.org/10.1016/0016-7037(94)90297-6).
- Konhauser, K.O., Hamade, T., Raiswell, R., Morris, R.C., Ferris, F.G., Southam, G., Canfield, D.E., 2002. Could bacteria have formed the Precambrian banded iron formations? *Geology* 30:1079–1082. [https://doi.org/10.1130/0091-7613\(2002\)030<1079:CBHFTP>2.0.CO;2](https://doi.org/10.1130/0091-7613(2002)030<1079:CBHFTP>2.0.CO;2).
- Konhauser, K.O., Planavsky, N.J., Hardisty, D.S., Robbins, L.J., Warchola, T.J., Haugaard, R., Lalonde, S.V., Partin, C.A., Oonk, P.B.H., Tsikos, H.,

- Lyons, T.W., Bekker, A., Johnson, C.M., 2017. Iron formations: A global record of Neoproterozoic to Palaeoproterozoic environmental history. *Earth-Sci. Rev.* 172:140–177. <https://doi.org/10.1016/j.earscirev.2017.06.012>.
- Large, R.R., Halpin, J.A., Lounejeva, E., Danyushevsky, L.V., Maslennikov, V.V., Gregory, D., Sack, P.J., Haines, P.W., Long, J.A., Makoundi, C., Stepanov, S., 2015. Cycles of nutrient trace elements in the Phanerozoic ocean. *Gond. Res.* 28:1282–1293. <https://doi.org/10.1016/j.gr.2015.06.004>.
- Leblanc, M., Lancelot, J., 1980. Interprétation géodynamique du domaine Pan-Africain de l'Anti-Atlas (Maroc) à partir de données géologiques et géochronologiques. *Can. J. Earth Sci.* 17:142–155. <https://doi.org/10.1139/e80-012>.
- Lechte, M. A., Wallace, M., van Smeerdijk Hood, A., Planavsky, N. 2018. Cryogenian iron formations in the proterogenic Kingston Peak Formation, California. *Pre. Res.* 310:443-462. <https://doi.org/10.1016/j.precamres.2018.04.003>.
- Lough, A. J. M., Klar, J. K., Homoky, W. B., Comer-Warner, S. A., Milton, J. A., Connelly, D.P., James, P.H., Mills, R.A., 2017. Opposing authigenic controls on the isotopic signature of dissolved iron in hydrothermal plumes. *Geochim. Cosmochim. Acta* 202:1–20. <https://doi.org/10.1016/j.gca.2016.12.022>.
- Lough, A.J.M., Homoky, W.B., Connelly, D.P., Comer-Warner, S.A., Nakamura, K., Abyaneh, M.K., Kaulich, B., Mills, R.A., 2019. Soluble iron conservation and colloidal iron dynamics in a hydrothermal plume. *Chem. Geol.* 511:225–237. <https://doi.org/10.1016/j.chemgeo.2019.01.001>.
- Lyons, T. W., Reinhard, C. T., and Planavsky, N. J., 2014. The rise of oxygen in Earth's early ocean and atmosphere. *Nature* 506:307–315. DOI:10.1038/nature13068.
- Manikyamba, C., Said, N., Santosh, M., Saha, A., Ganguly, S., Subramanyam, K.S.V., 2018. U enrichment and Th/U fractionation in Archean boninites: Implications for paleo-ocean oxygenation and U cycling at juvenile subduction zones. *J. Asian Earth Sci.* 157:187–197. <https://doi.org/10.1016/j.jseaes.2017.10.009>.

- McLennan, S.M., 1989. Rare Earth elements in sedimentary rocks: Influence of provenance and sedimentary processes. In: Lipin, B., McKay, G. (Eds.), *Geochemistry and mineralogy of the Rare Earth Elements*: Mineralogical Society of America, pp. 169–200.
- McLennan, S.M., 2001. Relationships between the trace element composition of sedimentary rocks and upper continental crust. *Geochem. Geophys. Geosyt.* 2: <https://doi.org/10.1029/2000GC000109>.
- Millet, M.-A., Baker, J.A., Payne, C.E., 2012. Ultra-precise stable Fe isotope measurements by high resolution multiple-collector inductively coupled plasma mass spectrometry with a  $^{57}\text{Fe}$ – $^{58}\text{Fe}$  double spike. *Chem. Geol.* 304-305:18–25. <https://doi.org/10.1016/j.chemgeo.2012.01.021>
- Mitra A., Elderfield H. and Greaves M. J., 1994. Rare earth elements in submarine hydrothermal fluids and plumes from the Mid-Atlantic Ridge. *Marine Chem.* 46:217–235. [https://doi.org/10.1016/0304-4203\(94\)90079-5](https://doi.org/10.1016/0304-4203(94)90079-5).
- Mohajerin, T.J., Helz, G.R., Johanneson, K.H., 2016. Tungsten–molybdenum fractionation in estuarine environments. *Geochim. Cosmo. Acta* 117:105–119. <https://doi.org/10.1016/j.gca.2015.12.030>.
- Mondillo, N., Balassone G., Forci, M., Chelle-Michou C., Cretella S., Mormone, A., Putzolu F., Santoro, F., Scognamiglio, G., Tarallo, M., 2019. Rare Earth Elements (REE) in Al- and Fe-(oxy)-hydroxides in bauxites of provence and Languedoc (Southern France): Implications for the potential recovery of REEs as by-products of bauxite mining. *Minerals* 9:504. <https://doi.org/10.3390/min9090504>.
- Mukherjee, I., Large, R.R., Bull, S., Gregory, D.G., Stepanov, A.S., Ávila, J., Ireland, T.R., Corkrey, R., 2019. Pyrite trace-element and sulfur isotope geochemistry of paleo-mesoproterozoic McArthur Basin: Proxy for oxidative weathering. *Am. Min.* 104:1256–1272. <https://doi.org/10.2138/am-2019-6873>.
- Ganno, S., Laure, N.T.E., Djibril, K.N.G., Arlette, D.S., Cyriel, M., Timoléon, N., Paul, N.J., 2017. A mixed seawater and hydrothermal origin of superior-type banded iron formations (BIF)-hosted Kouambo iron deposit, Paleoproterozoic Nyong Series Southwestern Cameroon: Constraints petrography and geochemistry. *Ore Geol.* 80:860–875.

- <https://doi.org/10.1016/j.oregeorev.2016.08.021>.
- Gartman, A., Findlay, A.J., 2020. Impacts of hydrothermal plume processes on oceanic metal cycles and transport. *Nat. Geosci.* 13:396–402. DOI:10.1038/s41561-020-0579-0.
- Percoits, E., Gingras, M.K., Barley, M.E., Kappler, A., Posth, N.R., Konhauser, K.O., 2009. Petrography and geochemistry of the Dales Gorge banded iron formation: Paragenetic sequence, source and implications for palaeo-ocean chemistry. *Pre. Res.* 72:163–187. <https://doi.org/10.1016/j.precamres.2009.03.014>.
- Planavsky, N., Bekker, A., Rouxel, O.J., Kamber, B., Hofmann, A., Knudsen, A., Lyons, T.W., 2010. Rare Earth Element and Yttrium compositions of Archean and Paleoproterozoic Fe formations revisited: new perspectives on the significance and mechanisms of deposition. *Geochim. Cosmochim. Acta* 74:6387–6405. <https://doi.org/10.1016/j.gca.2010.07.021>.
- Planavsky, N., Rouxel, O., Bekker, A., Hofmann, A., Little, C.T.S., Lyons., 2012. Iron isotope composition of some Archean and Proterozoic iron formations. *Geochim. Cosmo. Acta* 80:158–169. <http://dx.doi.org/10.1016/j.gca.2011.12.001>.
- Poulton, S.W., Krom, M.D., Raiswell, R., 2004. A revised scheme for the reactivity of iron (oxyhydr)oxide minerals towards dissolved sulfide. *Geochim. Cosmochim. Acta* 68:3703–3715. <https://doi.org/10.1016/j.gca.2004.03.012>.
- Poulton, S.W., Canfield, D.E., 2005. Development of a sequential extraction procedure for iron: Implications for iron partitioning in continentally derived particulates. *Chem. Geol.* 214:209–221. <https://doi.org/10.1016/j.chemgeo.2004.09.003>.
- Poulton, S.W., Canfield, D.E., 2011. Ferruginous Conditions: A dominant feature of the ocean through Earth's history. *Elements* 7:107–112. <https://doi.org/10.2113/gselements.7.2.107>.
- Radic A., Lacan, F., Murray, J.W., 2011. Iron isotopes in the seawater of the equatorial Pacific Ocean: New constraints for the oceanic iron cycle. *Earth and Planet. Sci. Letts.* 306:1–10. <https://doi.org/10.1016/j.epsl.2011.03.015>.

- Raiswell, R., Hardisty, D.S., Lyons, T.W., Canfield, D.E., Owens, J.D., Planavsky, N.J., Poulton, S.W., Reinhard, C.T., 2018. The iron paleoredox proxies: A guide to the pitfalls, problems and proper practice. *Am. J. Sci.* 318:491–526. DOI: <https://doi.org/10.2475/05.2018.03>.
- Reinhard, C.T., Planavsky, N.J., Robbins, L.J., Partin, C.A., Gill, B.C., Lalonde, S.V., Bekker, A., Konhauser, K.O., Lyong, T.W., 2013. Proterozoic ocean redox and biogeochemical stasis. *Proc. Natl. Acad. Sci. U.S.A.* 110:5357–5362. <https://doi.org/10.1073/pnas.1208622110>.
- Reinhard, C.T., Planavsky, N.J., Gill, B.C., Ozaki, K., Robbins, L.J., Lyons, T.W., Fischer, W.W., Wang, C., Cole, D.B., Konhauser, K.O., 2017. Evolution of the global phosphate cycle. *Nature* 541:386–389. DOI:10.1038/nature20772.
- Resing J. A., Sedwick P. N., German C. R., Jenkins W. J., Moffett J. W., Sohst B. M. and Tagliabue A., 2015. Basin-scale transport of hydrothermal dissolved metals across the South Pacific Ocean. *Nature* 523:U140–U200.
- Robbins, L.J., Konhauser, K.O., Warchola, T.J., Homann, M., Thoby, M., Foster, I., Mloszewski, A.M., Alessi, D.S., Lalonde, S.V., 2019. A comparison of bulk versus laser ablation trace element analysis in banded iron formations: Insights into the mechanisms leading to compositional variability. *Chem. Geol.* 506:197–224. <https://doi.org/10.1016/j.chemgeo.2018.12.036>.
- Rouxel, O., Dobbek, N., Ludden, J., Fouquet, Y., 2003. Iron isotope fractionation during oceanic crust alteration. *Chem. Geol.* 202:155–182. <https://doi.org/10.1016/j.chemgeo.2003.08.011>.
- Rouxel, O.J., Bekker, A., Edwards, K.J., 2005. Iron isotope constraints on the Archean and Paleoproterozoic ocean redox state. *Science* 307:1088–1091. <http://dx.doi.org/10.1126/science.1105692>.
- Rouxel, O., Shanks III, W.C., Bach, W., Edwards, K.J., 2008. Integrated Fe- and S-isotope study of seafloor hydrothermal vents at East Pacific rise 9–10°N. *Chem. Geol.* 252:214–227. <https://doi.org/10.1016/j.chemgeo.2008.03.009>.
- Rouxel, O., Toner, B.M., Manganini, S.J., German, C.R., 2016. Geochemistry

- and iron isotope systematics of hydrothermal plume fall-out at East Pacific Rise 9°50'N. *Chem. Geol.* 441:212–234. <https://doi.org/10.1016/j.chemgeo.2016.08.027>.
- Rouxel, O., Toner, B., Germain, Y., Glazer, B., 2018. Geochemical and iron isotopic insights into hydrothermal iron oxyhydroxide deposit formation at Loihi Seamount. *Geochim. Cosmo. Acta* 220:449-482. <https://doi.org/10.1016/j.gca.2017.09.050>.
- Sander, S. G. & Koschinsky, A., 2011. Metal flux from hydrothermal vents increased by organic complexation. *Nat. Geosci.* 4:145–150.
- Saunders, J.K., Rocap, G., 2016. Genomic potential for arsenic efflux and methylation varies among global *Prochlorococcus* populations. *The ISME J.* 10:197–209.
- Saquaque, A., Admou, H., Karson, J.A., Hefferan, K.P., Reuber, I., 1989. Precambrian accretionary tectonics in the Bou-Azzer El Graara region, Anti-Atlas. *Geology* 17:1107–1110. [http://dx.doi.org/10.1130/0091-7613\(1989\)017<1107:PATITB>2.0.CO;2](http://dx.doi.org/10.1130/0091-7613(1989)017<1107:PATITB>2.0.CO;2).
- Schofield, D.I., Horstwood, M.S., Pittfield, P.E.J., Crowley, Q.G., Wilkinson, A.F., Sidaty, H.C.O., 2000. Timing and kinematics of Eburnean tectonics in the central Reguibat shield, Mauritania. *J. Geol. Soc.* 163:549–560. <https://doi.org/10.1144/0016-764905-097>.
- Schrag, D.P., Higgins, J.A., Macdonald, F.A., Johnston, D.T., 2013. Authigenic carbonate and the history of the global carbon cycle. *Science* 339:540–543. DOI: 10.1126/science.1229578.
- Scott C, Lyons TW, Bekker A, Shen Y, Poulton SW, Chu X, Anbar AD., 2008. Tracing the stepwise oxygenation of the Proterozoic ocean. *Nature* 452:456–459. DOI:10.1038/nature06811.
- Scott, C., Lyons, T.W., 2012. Contrasting molybdenum cycling and isotopic properties in euxinic versus non-euxinic sediments and sedimentary rocks: Refining the paleoproxies. *Chem. Geol.* 324–325:19–27. <https://doi.org/10.1016/j.chemgeo.2012.05.012>.
- Severmann, M., Johnson, C.M., Beard, B.L., 2004. The effect of plume processes on the Fe isotope composition of hydrothermally derived Fe in the deep ocean as inferred from the Rainbow vent site, Mid-Atlantic Ridge, 36°14'N. *Earth Planet. Sci. Letts.* 225:63–76.

- <http://dx.doi.org/10.1016/j.epsl.2004.06.001>.
- Severmann, S., Lyons, T.W., Anbar, A., McManus, J., Gordon, G., 2008. Modern iron isotope perspective on the benthic iron shuttle and the redox evolution of ancient oceans. *Geology* 36:487–490. <https://doi.org/10.1130/G24670A.1>.
- Sharma, M., Polizzotto, M., Anbar, A.D., 2001. Iron isotope in hot spring along the Juan de Fuca Ridge. *Earth Planet. Sci. Letts.* 194:39–51. [https://doi.org/10.1016/S0012-821X\(01\)00538-6](https://doi.org/10.1016/S0012-821X(01)00538-6).
- Shields, G.A., Webb, G.E., 2004. Has the REE composition of seawater changed over geological time? *Chem. Geol.* 204:103–107. <https://doi.org/10.1016/j.chemgeo.2003.09.010>.
- Shields, G.A., Mills, B.J., 2017. Tectonic controls on the long-term carbon isotope mass balance. *Proc. Natl. Acad. Sci. U.S.A.* 114:4318–4323. <https://doi.org/10.1073/pnas.1614506114>.
- Singh, P., Rajamani, V., 2001. REE geochemistry of recent clastic sediments from the Kaveri floodplains, southern India: Implication to source area weathering and sedimentary processes. *Geochim. Cosmochim. Acta* 65:3093–3108. [https://doi.org/10.1016/S0016-7037\(01\)00636-6](https://doi.org/10.1016/S0016-7037(01)00636-6).
- Smedley P.L., Kinniburgh, D.G., 2002. A review of the source, behaviour and distribution of arsenic in natural waters. *Appl. Geochem.* 17:517–568. [https://doi.org/10.1016/S0883-2927\(02\)00018-5](https://doi.org/10.1016/S0883-2927(02)00018-5).
- Song, H., Jiang, G., Poulton, S. W., Wignall, P. B., Tong, J., Song, H., An, Z., Chu, D., Tian, L., She, Z., Wang, C., 2017. The onset of widespread marine red beds and the evolution of ferruginous oceans. *Nat. Comms.* 8:399. |DOI: 10.1038/s41467-017-00502-x.
- Sperling, E.A., Wolock, C.J., Morgan, A.S., Gill, B.C., Kunzmann, M., Halverson, G.P., Macdonald, F.A., Knoll, A.H., Johnston, D.T., 2015. Statistical analysis of iron geochemical data suggests limited late Proterozoic oxygenation. *Nature* 523:451–454. DOI:10.1038/nature14589.
- Stokey, L., 1970. Ferrozine—a new spectrophotometric reagent for iron. *Anal. Chem.* 42:779–781. <https://doi.org/10.1021/ac60289a016>.
- Stüeken, E. E. Kipp, M., Koehler, M. C., Buick, R. 2016. The evolution of Earth's biogeochemical nitrogen cycle. *Earth-Sci. Rev.* 160:220–239.

- <https://doi.org/10.1016/j.earscirev.2016.07.007>.
- Sun, Si., Konhauser, K.O., Kappler, A., Li, Y.-L., 2015. Primary hematite in Neoproterozoic to Paleoproterozoic oceans. *GSA Bulletin* 127:850–861.
- Thomas, R. J., Fekkak, A., Ennih, N., Errami, E., Loughlin, S.C., 2004. A new lithostratigraphic framework for the Anti-Atlas Orogen, Morocco. *39*, 217–226. <https://doi.org/10.1016/j.jafrearsci.2004.07.046>.
- Thompson, K.J., Kenward, P.A., Bauer, K.W., Warchola, T., Gauger, T., Martinez, R., Simister, R.L., Michiels, C.C., Llrós, M., Reinhard, C.T., Kappler, A., Konhauser, K.O., Crowe, S.A., 2019. Photoferrotrophy, deposition of banded iron formations, and methane production in Archean oceans. *Science Advances* 5: eaav2869. DOI: 10.1126/sciadv.aav2869.
- Tivey, M.K., 2007. Generation of seafloor hydrothermal fluids and associated mineral deposits. *Oceanography* 20:50–65. <https://doi.org/10.5670/oceanog.2007.80>.
- Toner, B. M., Fakra, S.C., Manganini, S.L., Santelli, C.M., Marcus, M.A., Moffett, J.W., Rouxel, O., German, C.R., Edwards, K.J., 2009. Preservation of iron(II) by carbon-rich matrices in a hydrothermal plume. *Nat. Geosci.* 2:197–201. DOI:10.1038/ngeo433.
- Tostevin, R., Shields, G.A., Frabuck, G.M., He, T., Clarkson, M.O., Wood, R.A., 2016. Effective use of cerium anomalies as a redox proxy in carbonate-dominated marine settings. *Chemical Geology*, 438, 146-162. <https://doi.org/10.1016/j.chemgeo.2016.06.027>.
- Toth, J.R., 1980. Deposition of submarine crusts rich in manganese and iron. *Geol. Soc. Amer. Bull.* 91:52–60. [https://doi.org/10.1130/0016-7606\(1980\)91<44:DOSCRI>2.0.CO;2](https://doi.org/10.1130/0016-7606(1980)91<44:DOSCRI>2.0.CO;2).
- Triantafyllou, A., Berger, J., Baele, J.-M., Diot, H., Ennih, N., Plissart, G., Monnier, C., Watlet, A., Bruguier, O., Spagna, P., Vandycke, S., 2016. The Tachakoucht-Iriri-Tourtit arc complex (Moroccan Anti-Atlas): Neoproterozoic records of polyphased subduction accretion dynamics during the Pan-African orogeny. *J. Geody.* 96:81–103. <https://doi.org/10.1016/j.jog.2015.07.004>.
- Tribovillard, N., Algeo, T.J., Lyons, T., Riboulleau, A., 2006. Trace metals as paleoredox and paleoproductivity proxies: An update. *Chem. Geol.* 232:12–32. <https://doi.org/10.1016/j.chemgeo.2006.02.012>.

- Visscher, P.T., Gallagher, K.L., Bouton, A., Farias, M.E., Kurth, D., Sancho-Tomás, M., Philippot, P., Somogyi, A., Medjoubi, K., Vennin, E., Bourillot, R., 2020. Modern arsenotrophic microbial mats provide an analogue for life in the anoxic Archean. *Comm. Earth Environ.* 1:24. <https://doi.org/10.1038/s43247-020-00025-2>.
- Wani, H., Mondal, M.E.A., 2011. Evaluation of provenance, tectonic setting and paleoredox conditions of the Meso-Neoproterozoic basins of the Bastar craton, Central Indian Shield: Using petrography of sandstones and geochemistry of shales. *Lithosphere* 3:143-154. <https://doi.org/10.1130/L74.1>.
- Weber, K.A., Achenbach, L.A., Coates, J.D., 2006. Microorganisms pumping iron: Anaerobic microbial iron oxidation and reduction. *Nature Rev. Microbiol.* 4:752–764. <http://dx.doi.org/10.1038/nrmicro1490>.
- Wu, D., Purnomo, B.J., Sun, S., 2017. As and Sb speciation in relation with physico-chemical characteristics of hydrothermal waters in Java and Bali. *J. Geochem. Exp.* 173:85–91. <https://doi.org/10.1016/j.gca.2016.12.003>.
- Wurl, O., Zimmer, L., Cutter, G.A., 2013. Arsenic and phosphorus biogeochemistry in the ocean: Arsenic species as proxies for P-limitation. *Limnol. Oceanogr.* 58: 729–740. <https://doi.org/10.4319/lo.2013.58.2.0729>.
- Yan, B., Zhu, Z.-K., Tang, S.-H., Zhu, M.-Y., 2010. Fe isotope characteristics of Neoproterozoic BIF in Guangxi Province and its implications. *Acta Geol. Sin.* 84:1080–1086.
- Yücel, M., Gartman, A., Chan, C. S., Luther, G. W., 2011. Hydrothermal vents as a kinetically stable source of iron-sulphide-bearing nanoparticles to the ocean. *Nat. Geosci.* 4:367–371. DOI:10.1038/ngeo1148.
- Zhang, X., Sigman, D.M., Morel, F.M.M., Kraepiel, A.M.L., 2014. Nitrogen isotope fractionation by alternative nitrogenases and past ocean anoxia. *Proc. Natl. Acad. Sci. U.S.A.* 111:4782–4787. <https://doi.org/10.1073/pnas.1402976111>.
- Zegeye, A., Bonneville, S., Benning, L.G., Sturm, A., Fowle, D.A., Jones, C., Canfield, D.E., Ruby, C., MacLean, L.C., Nomosatryo, S., Crowe, S.A., Poulton, S.W., 2012. Green-rust formation controls nutrient availability in

a ferruginous water column. *Geology* 40:599–602. <https://doi.org/10.1130/G32959.1>.

Zeng, Z., Wang, X., Qi, H., Zhu, B., 2018. Arsenic and Antimony in Hydrothermal plumes from the Eastern Manus Basin, Papua New Guinea. *Geofluids* 6079586. <https://doi.org/10.1155/2018/6079586>.

Zhou, J.L., Li, X.H., Tang, G.Q., Gao, B.Y., Bao, Z.A., Ling, X.X., Wu, L.G., Lu, K., Zhu, Y.S., Liao, X., 2018. Ca. 890 Ma magmatism in the northwest Yangtze block, South China: SIMS U-Pb dating, in-situ Hf-O isotopes, and tectonic implications. *J. Asian Earth Sci.* 151, 101–111. <https://doi.org/10.1016/j.jseaes.2017.10.029>.

Fig. 1: Geological setting and structural units of the Proterozoic basement of the Anti-Atlas and location of the studied area. (a) Geological sketch map of the Proterozoic basement of the Anti-Atlas showing the three lithostructural domains and the studied area. SAFZ: South Atlas Fault Zone, AAFZ: Anti-Atlas Fault Zone; inset showing the location of the Anti-Atlas domain, (b) simplified map of the Pan-African craton margin strata in the central Anti-Atlas showing location of the studied section (Ag). Tl: Taliwine, Tz: Tazenakht. (Modified from Bouougri et al., 2020).

Fig. 2. (a) Stratigraphic framework of the craton margin successions in the central part of the Anti-Atlas subdivided into Pre-Pan-African and Pan-African megacycles (Bouougri et al., 2016, modified from Bouougri and Saquaque, 2004). Key radiometric ages in blue and red from Bouougri et al. (2020). (b) Simplified measured section showing the sampled horizons including Fe-rich deposits of Wanimzi Fm. and clastic stromatolites of Imi n'Tizi Fm.

Fig. 3. Field features of Fe-bearing rocks of Wanimzi Formation: (a) General view within the upper part of Wanimzi Formation showing the transition from Fe-bearing interval with purple-red color and the overlying white interval without Fe. Dashed blue line indicates the sampled section. (b) Location of the sampled layers, numbered within the studied section shown in (a). (c) Detail within the sampled section showing several Fe-rich thin layers and

interbeds consisting of storm deposits with Hummocky cross-stratification (HCS); scale 14.5 cm. (d) Thick Fe-rich and isolated storm bed occurring within heterolithic deposits. Hammer scale is 33 cm.

Fig. 4. Examples of sedimentary and microbial mat-related features of the siliciclastic Wanimzi and Imi n'Tizi Formations (e.g., Bouougri and Porada, 2002, Porada and Bouougri, 2007; Bouougri and Porada, 2011). (a-b) Sandstones with bedding planes showing symmetrical and asymmetrical ripples. (c) Kinneyia-type wrinkles occurring as patches on bedding surfaces of storm deposits. (d) Sand-filled spindle-shaped and randomly oriented cracks. (e) Mat-deformation structures occurring as curved and often bifurcating ridges. (f) Bedding surface preserving subrounded and flat sand clasts. (g-h) Siliciclastic biolaminites (stromatolites), showing domal features on bedding surface (h) and in cross section (g). Scale: (a-e-g) hammer is 33 cm long, (d-f) and (h) coin is 2.4 cm and 2 cm in diameter, respectively.

Fig. 5. Examples of thin section photomicrographs of sampled facies viewed in cross polarized light. (a) Siliciclastic microbial mats at the Imi n'Tizi shallow water stromatolite-rich Formation, showing fine-grained and coarse-grained alternating layers. (b) magnification of the red box in panel (a) showing the characteristic siliciclastic coarse-grained laminae composed mainly of quartz grains alternating with a thinner fine-grained clay-rich layer represented by the red arrow. c-f, Siliciclastic iron-rich deposits showing various well-sorted rounded and sub-angular quartz grains floating in a black iron-rich matrix in the Fe-rich lithologies of the Wanimzi Formation. g-i, Examples of thin section photomicrographs for the siliciclastic carbonate-rich facies from the Taghdout Formation, characterized by ooids, quartz, carbonates and iron oxides. Ooid-peloid grainstone, the iron ooids (1) are made of microcrystalline calcitic laminae with radially arranged crystals (light rings) and iron enriched thinner laminae (dark). (2) peloids. (3) Oolites relicts showing the dissolution of the original structure and its replacement by drusy calcite crystals, indicating a neomorphism process (advanced diagenesis). (4) quartz. (5) calcite. The presence of intraclasts (red dashed line) indicate a shallow marine environment.

Fig. 6. Redox sensitive trace element, organic carbon ( $C_{org}$ ) and  $d^{13}C_{org}$  distribution up the studied stratigraphic section. (a-d), Trace element distribution for Zn, Cu, Mo, Co, As, V, U, Sb. e, Bulk iron enrichment averaging 22 wt.%, 0.73 wt.% and 1.1 wt.% in the Wanimzi Formation, the overlying siliciclastic stromatolitic succession and in the underlying siliciclastic carbonates from the Taghdout Formation, respectively. f, Zn/Co ratios. g, Mo/W ratio. h, Th/U ratio. i,  $C_{org}$  concentration. j, Carbon isotope distribution in  $C_{org}$ . Sil Car= Siliciclastic carbonates.

Fig. 7. PAAS-normalized REE+Y distribution across the succession. a, REE+Y patterns in the overlying Imi n'Tizi stromatolitic formation. b, REE+Y distribution in the siliciclastic iron-rich Wanimzi Formation. c, REE+Y distribution in the underlying Taghdout Formation carbonates.

Fig. 8. Relationship between hydrothermally enriched REES (Nd, La, Ga, Eu and Ce) and non-hydrothermally enriched REE (Pr), and Zr and Th typically enriched in siliciclastic deposits.

Fig. 9. (a) Eu anomalies calculated as  $(Eu/Eu^*)_{SN1} = Eu_{SN} / (0.67Sm_{SN} + 0.33Tb_{SN})$  and as  $(Eu/Eu^*)_{SN2} = 2 \times Eu_{SN} / (Sm_{SN} + Gd_{SN}) - (Eu/Eu^*)_{SN1}$  and  $(Eu/Eu^*)_{SN2}$  to correct for anomalously high Gd and Tb concentrations, respectively. (b) Light REE (LREE) to high REE (HREE) ratios. (c) Y/Ho ratios. (d),  $(La/Y)_{bSN}$  ratio. (e)  $(Tb/Yb)_{SN}$  ratio. (f)  $(Pr/Yb)_{SN}$  ratio. (g),  $(Sm/Yb)_{SN}$  ratio. (h)  $(Eu/Sm)_{SN}$  ratio. (i)  $(Gd/Gd^*)_{SN}$  ratio. SN=Shale normalized.

Fig. 10. Water column redox conditions determined by REE and Fe-based redox reconstruction. a, Cerium anomaly calculated as  $(Ce/Ce^*)_{SN} = Ce_{SN} / (0.5Pr_{SN} + 0.5La_{SN})$  and  $(Pr/Pr^*)_{SN} = Pr_{SN} / (0.5Ce_{SN} + 0.5Nd_{SN})$ . Black rings, blue diamonds and purple filled rings represent the Imi n'Tizi stromatolitic deposit, Wanimzi Formation and the Taghdout carbonates, respectively. With the exception (ironstone) of sample AG12 and CAB (Taghdout carbonate) all data points record true negative Ce Anomalies. b-c, Iron-based bottom water

redox reconstruction. S1-S4= Imi n'Tizi stromatolitic deposit. AG01-AG17=Wanimzi Formation. CA1, CA2, CAB= Taghdout carbonates.

Fig. 11. Distribution of iron concentrations and isotopic distribution. a,  $\delta^{56}\text{Fe}$  and  $\delta^{57}\text{Fe}$  distribution in the iron-rich and siliciclastic stromatolitic rocks. b, Bulk iron dynamics showing that at less than 5 wt.% Fe concentration (vertical line),  $\delta^{56}\text{Fe}$  values are more positive and increasingly positive above this value. Above this line strong fractionation of iron produces more negative  $\delta^{56}\text{Fe}$  values. The asterisks depict two samples (AG08 and AG12) that deviate from the latter observations and are linked to the enrichment of LREE levels, as depicted by LREE/HREE ratios and  $(\text{La}/\text{Yb})_{\text{CN}}$  (See Figure 9b and 9d). c,  $\delta^{56}\text{Fe}$  distribution in sedimentary marine iron formations deposited at key intervals across Earth history adapted from Planavsky et al. (2012) and Halverson et al. (2011) relative to the black ringed values obtained in this study. SS=siliciclastic stromatolites.

Fig. 12. Relationship between iron and As (a), iron and V (b) and Mo and As (c) in the Wanimzi ironstones.

Fig. 13. Conceptual model for the formation of the Wanimzi iron-rich shallow marine ironstone deposit on the Tonian passive continental margin of the WAC.

Table 1. XRD mineralogical data (+=Detected; -=Not detected; ?=Uncertain).

	Lithology	Hematite	Magnetite	Gothite	Ankerite	Siderite	Albite	Kaolinite	Quartz	Chlorite	Dolomite	Calcite	Illite	K-feldspar
S1	Stromatolitic	+	-	-	?	-	+	+	+	-	?	+	+	+
S2	Stromatolitic	+	-	-	?	-	+	+	+	-	?	+	+	+
S3	Stromatolitic	+	-	-	-	-	+	-	+	-	-	-	+	+
S4	Stromatolitic	+	-	-	-	-	+	-	+	-	-	-	+	+
AG17	Iron-Quartz	+	-	-	-	-	+	-	+	-	-	-	+	+
AG16	Iron-Quartz	+	-	-	-	-	-	-	+	-	-	-	+	+
AG1	Iron-Quartz	+	-	-	-	-	-	-	+	-	-	-	+	+

5														
A	Iron-	+	-	-	-	-	-	-	+	-	?	?	+	+
G1	Quartz													
4														
A	Iron-	+	-	-	-	-	-	-	+	-	-	?	+	+
G1	Quartz													
3														
A	Iron-	+	-	-	-	-	-	-	+	-	?	-	+	-
G1	Quartz													
2														
A	Iron-	+	-	-	-	-	-	-	+	-	-	-	-	+
G1	Quartz													
1														
A	Iron-	+	-	-	-	-	-	-	+	-	-	-	+	-
G1	Quartz													
0														
A	Iron-	+	-	-	-	-	-	-	+	-	-	-	-	-
G0	Quartz													
9														
A	Iron-	+	-	-	-	-	-	-	+	-	-	-	+	+
G0	Quartz													
8														
A	Iron-	+	-	-	?	-	-	-	+	-	?	?	+	+
G0	Quartz													
7														
A	Iron-	+	-	-	?	-	-	-	+	-	-	?	+	+
G0	Quartz													
6														
A	Iron-	+	-	-	-	-	-	-	+	-	-	-	?	-
G0	Quartz													
5														
A	Iron-	+	-	-	-	-	-	-	+	-	-	-	+	-
G0	Quartz													
4														
A	Iron-	+	-	-	-	-	-	-	+	+	?	-	-	-
G0	Quartz													
3														
A	Iron-	+	-	-	-	?	-	+	+	-	-	-	-	-
G0	Quartz													
2														
A	Iron-	+	-	-	-	-	-	-	+	-	-	-	-	-
G0	Quartz													
1														
A	Iron-	+	-	-	-	-	-	-	+	-	-	-	+	-
G0	Quartz													
CA	Carbo	+	-	-	-	-	-	-	+	-	+	+	+	-
1	nates													
CA	Carbo	+	-	-	-	-	-	-	+	-	+	+	+	+
2	nates													
CA	Carbo	+	-	-	-	-	-	-	+	-	+	+	+	+
B	nates													

Table 2. Trace metal(loid) distribution. With the exception of Au measured in ppb concentrations are in ppm. Total Fe was measured by the ferrozine method (Stokey, 1970). Av. UCC (Average Upper Continental Crust concentrations (McLennan, 2001)). All UCC units are in ppm with the exception of Au, Bi, and Pd that are in ppb. AG/SS (Average concentration in iron-rich facies relative to average siliciclastic stromatolitic facies). AG/CAB (Average concentration in iron-rich facies relative to average siliciclastic carbonate lithologies). AG/UCC (Average iron-rich concentrations relative to average upper continental crust concentrations). SS/UCC (Average siliciclastic stromatolitic facies concentration relative to average upper continental crust). CAB/UCC (Average siliciclastic carbonate concentration relative to upper continental crust concentrations).

	As	Au	Ba	Co	Cu	Fe	Hf	Ga	Mo	Nb	Ni
Av. UCC	1.5	1.8	550	17	25	3500	5.8	17	1.5	12	44
S1	3.4	1.6	421	72.4	13.3	4741	13.6	7.7	0.2	6.8	1.6
S2	0.8	1.8	337	68.8	13.7	7198	17.3	8.6	0.2	7.9	2
S3	0.6	0.8	459	65.2	13.2	7292	7.4	11.3	0.2	8.2	2.1
S4	1.6	<0.5	568	39.7	12.1	7292	10.5	12.8	0.2	9.3	1.5
AG17	3.4	<0.5	362	80.2	59.4	3404	6.9	11.5	0.3	6.5	22.8
AG16	33.7	1.3	130	50.2	40.6	3843	5.3	2.6	1.5	2.4	10.1
AG15	6.9	<0.5	156	129.6	12.9	5659	4.6	2.8	0.6	2.8	3.7
AG14	1.9	0.7	319	194.1	13.9	1335	11.6	7.3	0.4	4.6	4.3
AG13	40.1	1	218	114	20.4	1578	8.4	9.3	2.6	5.2	17.2
AG12	4.1	<0.5	381	61.6	8.5	1985	5.6	10.2	1	7.5	3.9
AG11	86.9	1.6	37	29.7	2.8	5202	0.8	2.8	8.9	1.6	12.9
AG10	26.8	2.3	242	64.2	5.7	1011	4.9	6.6	2	5.4	5
AG09	111.3	3.4	57	9.9	4.2	5837	0.8	3.5	6.9	4	9.9
AG08	48.4	1.7	46	80.8	4.3	2288	0.9	5.2	4.8	2.9	6.7
AG07	66.1	0.9	350	86.6	2.4	2471	5.7	8.7	0.3	5.5	10.1
AG06	3.3	<0.5	289	148.7	35.7	1893	4.4	4.5	0.4	2.8	18.1
AG05	2.2	<0.5	539	64.5	7.2	6039	7.2	22.1	0.3	13.4	18.9

AG04	10.6	1.1	184	110.5	23.3	71295	4.7	6.1	1.1	3.2	28.6
AG03	10.6	1.1	336	43	23.3	617303	0.5	5.7	1.1	2.8	28.6
AG02	43.2	2.8	215	37.3	20.1	559723	1.2	3.8	3.4	2.1	31.1
AG01	22	2.6	423	39	120.7	535025	0.6	5.1	2.2	1.4	38.6
AG0	3.5	1.5	491	42.4	29.4	44948	8.2	17	0.3	10.3	12.5
CA1	3.4	9.9	1606	21.1	2.3	13348	1	1.6	0.1	1.4	1.5
CA2	0.1	1.2	383	22.3	10	6458	2.5	2.9	2.2	1.5	3.3
CAB	6.4	1.4	215	38.9	4.6	11872	2.9	2.3	0.1	1.8	2.2
AG/SS	18.2	1.2	0.6	1.3	1.8	33.7	0.4	0.7	10.6	0.6	8.7
AG/CAB	8.8	0.4	0.4	2.8	4.3	21.2	2.1	3.3	2.6	3	6.7
AG/UC	19.4	0.9	0.5	4.5	1	64	0.8	0.4	1.4	0.4	0.4
SS/UC	1.1	0.8	0.8	3.6	0.5	1.9	2.1	0.6	0.1	0.7	0.04
CAB/UC	2.2	2.3	1.3	1.6	0.2	3	0.4	0.1	0.5	0.1	0.05
	Pb	Rb	Sb	Sr	Ta	Th	U	V	W	Zn	Zr
UCC	0.5	112	0.2	350	1	10.7	2.8	107	2	71	190
S1	0.9	94.8	0	17.5	1.4	8.2	1.7	28	448.1	1	18.6
S2	1	95.5	0	16.9	1.3	9.5	0.9	34	491.1	0	21.6
S3	1.2	126.6	0	29.7	1.1	9.1	0.5	41	44.8	2	14.9
S4	1.2	151.1	0.2	21.9	1.1	10.6	1	42	242.6	1	20.3
AG17	1	104.7	0.1	13.3	1.2	9	1.8	56	517.7	8	23.4
AG16	2	22.3	0.9	12.1	0.7	3.7	1.1	17	332.8	10	31.7
AG15	1.8	29.6	0.2	11.3	1.8	3.5	1.3	11	936.5	3	8.9
AG14	0.8	71.4	0.1	17	2.7	6.7	0.9	30	1332.5	1	13.2
AG13	4.9	87.9	2.4	13.1	1.6	6.6	2.1	37	749.9	4	14.2
AG12	0.7	117.4	0.3	16	1.3	8.4	2.2	54	461.3	1	15
AG11	3.4	15.8	5.3	5	0.4	2.8	1.2	74	172.9	2	7.5

AG10	2.9	69.8	2	13	1.2	5.8	0.4	31	486. 2	2	12. 7
AG09	11.3	25.3	7.8	6.8	0.2	2.2	2.3	81	36.3	2	13. 9
AG08	4.3	37.3	3.6	4.5	1	4.5	1	74	580. 5	1	21. 1
AG07	1.2	84.8	0.1	13.6	1.6	6.4	2.2	44	663. 9	4	13. 4
AG06	0.8	47.4	0	14.1	2.2	3	1.9	24	1250 .8	7	7.2
AG05	1.5	186. 7	0.3	20.8	1.8	16	2.3	11 0	484. 3	7	17. 2
AG04	1.7	36.6	0.3	8.6	1.9	4.3	1	47	941. 9	10	12. 9
AG03	1.7	5.5	2.5	9.8	0.2	2	2.2	17 3	75.2	10	14. 4
AG02	5.1	3	2.8	8.8	0.3	2.5	1.9	17 2	180. 8	11	27. 6
AG01	3.3	3.5	1.4	11	0.2	1.5	1	13 9	135. 1	15	15. 4
AG0	1.6	143. 3	0.3	20.8	1.7	12.5	2.5	95	516. 2	4	30. 9
CA1	14.6	21.5	0.1	1074 .4	0.3	10.7	0.4	8	128. 3	8	25
CA2	10	44	0	790. 8	0.3	7.7	0.4	9	111. 9	3.3	18. 4
CAB	11	29.1	0	1033 9	0.4	11.7	0.4	<8	227. 8	9	20. 8
AG/SS	2.6	0.5	33. 8	0.6	1	0.6	1.6	2	1.8	5.7	0.9
AG/CAB	0.2	1.9	50 7	0.01	3.7	0.6	4.1	8.3	3.5	0.8	0.8
AG/UC C	5.6	0.5	8.4	0.03	1.2	0.5	0.6	41. 6	273. 7	0.1	0.1
SS/UC C	2.2	1	0.3	0.1	1.2	0.9	0.4	21. 3	153. 3	0.0 1	0.1
CAB/UC CC	23.7	0.3	0.2	2.8	0.3	0.9	0.1	5	78	0.1	0.1

Table 3. Carbon, iron, and oxygen isotopic data

	Lithology	$\delta^{13}\text{C}_{\text{carb}}$ onate (‰ VPDB)	1s d	$\delta^{18}\text{O}_{\text{carb}}$ onate (‰ VPDB)	1s d	Carbo nate (%wt)	$\delta^{13}\text{C}$ org (‰ VPD B)	1s d	$\text{C}_{\text{org}}$ (wt %)	$\delta^{56}\text{F}$ e (‰ IRM M)	2s d	$\delta^{57}\text{F}$ e (‰ IRM M)	2s d
S1	Stromato litic	-1.84	0. 10	-13.13		0.02	- 31.8 0	0. 49	0.0 1	0.61	0. 05	0.86	0. 14
S2	Stromato litic	ND*	-	ND*	-	0.01	- 30.1 6	0. 49	0.0 1	0.45	0. 05	0.70	0. 15
S3	Stromato litic	-0.33	0. 22	-4.00	0. 17	0.02	- 28.1 3	0. 49	0.0 2	0.57	0. 05	0.88	0. 15
S4	Stromato litic	-4.50	0. 18	-9.29	0. 16	0.01	- 27.8 7	0. 49	0.0 1	0.45	0. 05	0.66	0. 14
AG 17	Iron- Quartz	ND*	-	ND*	-	ND*	- 29.9 7	0. 49	0.0 3	-	0. 05	-	0. 14
AG 16	Iron- Quartz	ND*	-	ND*	-	ND*	- 27.4 4	0. 49	0.0 1	-	0. 05	-	0. 14
AG 15	Iron- Quartz	ND*	-	ND*	-	ND*	- 31. 2	0. 49	0.0 3	-	0. 05	-	0. 14
AG 14	Iron- Quartz	-8.72	-	-12.788	-	0.02	- 29.8 2	0. 49	0.0 4	0.03	0. 05	0.02	0. 14
AG 13	Iron- Quartz	ND*	-	ND*	-	ND*	- 27.8 1	0. 49	0.0 3	-	0. 05	-	0. 14
AG 12	Iron- Quartz	ND*	-	ND*	-	ND*	- 30.6 4	0. 49	0.0 2	0.26	0. 05	0.52	0. 14
AG 11	Iron- Quartz	ND*	-	ND*	-	ND*	- 28.3 8	0. 49	0.0 1	-	0. 05	-	0. 14
AG 10	Iron- Quartz	ND*	-	ND*	-	ND*	- 29.1 5	0. 49	0.0 2	0.03	0. 05	0.08	0. 14
AG 09	Iron- Quartz	ND*	-	ND*	-	ND*	- 26.1 2	0. 49	0.0 2	0.06	0. 05	0.03	0. 14
AG 08	Iron- Quartz	ND*	-	ND*	-	ND*	- 30.2 7	0. 49	0.0 2	0.35	0. 05	0.54	0. 14
AG 07	Iron- Quartz	ND*	-	ND*	-	ND*	- 30.7 4	0. 49	0.0 2	0.06	0. 05	0.14	0. 14
AG 06	Iron- Quartz	ND*	-	ND*	-	ND*	- 33.0 3	0. 49	0.0 2	-	0. 05	-	0. 14
AG 05	Iron- Quartz	ND*	-	ND*	-	ND*	- 29.3 3	0. 49	0.0 3	0.11	0. 05	0.27	0. 14
AG 04	Iron- Quartz	-8.72	0. 21	-12.788	0. 21	ND*	- 28.5 6	0. 49	0.0 2	-	0. 05	-	0. 14
AG 03	Iron- Quartz	ND*	-	ND*	-	ND*	- 28.8 2	0. 49	0.0 2	0.07	0. 05	0.30	0. 14
AG 02	Iron- Quartz	ND*	-	ND*	-	ND*	- 27.5 0	0. 49	0.0 1	-	0. 05	-	0. 14

AG 01	Iron- Quartz	ND*	-	ND*	-	ND*	-	0.	0.0	-	0.	-	0.
							22.9	49	1	0.09	05	0.08	14
							3						
AG 0	Iron- Quartz	ND*	-	ND*	-	ND*	-	0.	0.0	0.15	0.	0.21	0.
							29.6	49	4		05		14
							2						
CA 1	Carbonat es	-0.77	0.	-14.50	0.	75	-	0.	0.0	ND	0.	ND	0.
			13		10		26.4	49	4		05		14
							4						
CA 2	Carbonat es	0.11	0.	-13.28	0.	50	-	0.	0.0	ND	0.	ND	0.
			07		06		27.4	49	4		05		14
							1						
CA B	Carbonat es	-0.18	0.	-14.30	0.	75	-	0.	0.0	ND	0.	ND	0.
			05		05		28.4	49	6		05		14
							1						

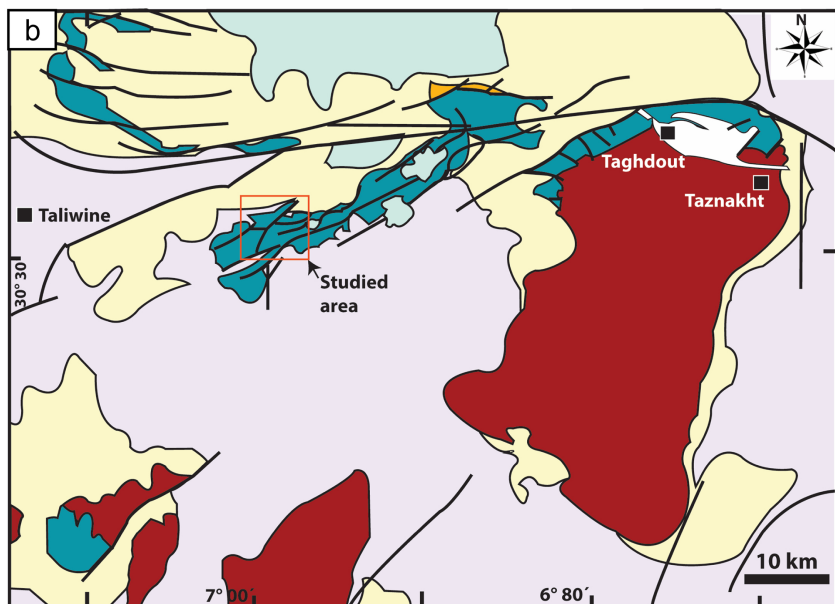
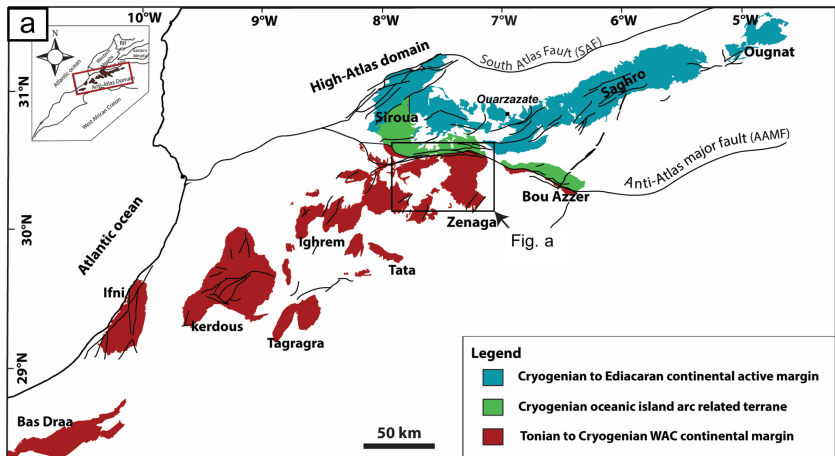
ND=Not determined

ND\*=Not determined because of extremely low carbonate content

Table 4. Rare Earth Element +Yttrium. S1-S2=Siliciclastic supracrustal mats. AG17-AG0=Wanimzi Formation. CA1,2,B=Taghdout carbonates.

	Lithology	La	Ce	Pr	Nd	Sm	Eu	Gd	Tb	Dy	Y	Hf	Er	Tm	Yb	Lu	ΣRE E+Y	ΣR EE
S1	Stromatolite	2.66	52.2	5.46	19.8	3.15	0.59	2.57	0.47	3.1	0.86	0.68	2.13	0.13	2.13	0.33	138.1	11.95
S2	Stromatolite	2.65	56.9	6.11	22.8	3.76	0.75	3.24	0.55	3.4	0.96	0.33	2.53	0.37	2.62	0.42	152.3	13.07
S3	Stromatolite	3.54	67.1	7.12	25.2	3.73	0.65	2.77	0.22	2.1	0.99	0.99	1.28	0.27	1.41	0.31	164.8	14.99
S4	Stromatolite	3.26	66.4	7.46	28.5	4.71	0.88	4.16	0.33	3.3	0.33	0.33	2.9	0.69	2.37	0.37	175.6	15.33
A G1 7	Iron- Quartz z	1.76	35.9	4.45	19.3	6.2	1.66	8.38	1.1	4.5	2.3	2.49	2.09	0.99	1.47	0.7	127.5	10.41
A G1 6	Iron- Quartz z	1.28	27.6	3.1	12.8	3.84	1.22	8.93	1.6	5.17	3.4	3.46	2.35	0.65	1.43	0.33	114.5	82.8
A G1 5	Iron- Quartz z	1.07	23.7	2.75	10.8	2.56	0.77	2.53	0.27	1.7	0.9	0.94	0.81	0.24	0.44	0.1	77.6	68.7
A G1 4	Iron- Quartz z	1.35	28.4	2.79	10.7	1.72	0.48	1.87	0.54	2.32	1.42	0.79	1.55	0.48	0.84	0.44	78.2	65.0
A G1 3	Iron- Quartz z	2.32	54.4	5.3	19.3	3.28	0.88	3.11	0.87	2.48	0.84	0.22	1.55	0.38	0.56	0.55	131.1	11.69
A G1 2	Iron- Quartz z	4.16	79.7	7.42	26.1	1.08	0.88	3.14	0.33	2.5	0.54	0.44	1.66	0.44	0.55	0.55	185.1	17.01
A G1 1	Iron- Quartz z	3.85	10.15	1.3	5.3	2.15	0.88	2.54	0.88	1.8	0.53	0.16	0.71	0.18	0.18	0.1	37.7	30.2
A G1 0	Iron- Quartz z	1.47	35.7	3.67	14.7	3.27	0.75	3.05	0.45	2.66	1.78	0.78	1.44	0.91	1.32	0.2	95.2	82.5
A G0 9	Iron- Quartz z	1.53	39.6	4.05	17.6	4.78	1.99	4.67	0.88	3.49	2.55	1.52	1.33	0.61	1.14	0.4	108.3	94.4
A G0 8	Iron- Quartz z	5.68	23.8	28.1	15.2	5.78	0.99	9.35	2.15	6.97	2.1	0.2	1.62	0.13	0.13	0.1	615.9	59.48
A G0 7	Iron- Quartz z	1.36	4.2	15.9	2.98	0.52	0.99	2.52	0.82	2.34	0.44	0.61	1.32	0.11	0.22	0.2	100.83	87.4
A G0 6	Iron- Quartz z	9.18	18.1	5.8	8.76	1.4	0.79	1.79	0.55	1.42	0.22	0.69	0.71	0.17	0.12	0.2	55.6	48.8
A G0 5	Iron- Quartz z	2.51	5.8	22.2	4.79	0.99	0.33	3.79	0.44	3.17	0.22	0.44	1.99	0.78	0.8	0.2	140.55	12.8
A G0 4	Iron- Quartz z	6.13	9.2	62.2	7.61	2.7	0.2	4.7	0.63	2.99	0.88	0.88	1.75	0.75	0.55	0.1	55.6	42.7

A	Iron-	5.	12	1.	6.	2.	0.	4.	0.	3.	1	0.	1.	0.	0.	0.	53.	39
G0	Quart	5		42	1	54	8	39	6	0	4.	5	2	1	8	1	9	.5
3	z						1		6	8	4	5	6	5	7	2		
A	Iron-	5.	10	1.	6.	2.	1.	6.	1.	5.	2	0.	2.	0.	1.	0.	73.	45
G0	Quart	2	.6	4	7	99	0	39	0	2	7.	9	2	2	4	1	3	.7
2	z						4		4	8	6	3	8	4	3	9		
A	Iron-	3.	6.	0.	4.	2.	0.	5.	0.	3.	1	0.	1.	0.	0.	0.	46.	30
G0	Quart	1	2	91	6	42	8	43	7	3	5.	5	3	1	8	1	1	.7
1	z						4		8	8	4	8	3	4	9	1		
A	Iron-	3	61	7.	30	9.	2.	12	1.	6.	3	1.	2.	0.	2.	0.	199	16
G0	Quart	0.	.8	18		15	2	.3	4	1	0.	1	7	3	4	3	.1	8.
	z	9					5	2	6	8	9	1	3	7	1	6		2
CA	Carbo	3	71	6.	24	4.	1.	4.	0.	4.	2	0.	2.	0.	2.	0.	186	16
1	nate	5.	.1	55	.6	82	1	82	7	7	5	9	9	4	9	4	.3	1.
		1					1		7	8		4	3	1	3			2
CA	Carbo	2	61	5.	21	4.	0.	3.	0.	3.	1	0.	0.	1.	0.	152	13	
2	nate	8.	.6	77	.3	03	8	45	5	2	8.	6	2	2	8	2	.2	3.
		1					1		2	5	4	4	4	6	3	8		8
CA	Carbo	4	86	8.	30	5.	0.	4.	0.	3.	2	0.	2.	0.	2.	0.	208	18
B	nate	2.		14	.2	29	9	42	6	9	0.	7	2	3	1	3	.9	8.
		7					6		8	5	8	7	1	3	3	3		1



**Legend**

- Tonian /Cryogenian arc terrane (ca. 770 to 640 Ma)
- Upper Paleoproterozoic to Cryogenian continental margin strata
- Paleoproterozoic Eburnean basement (WAC)
- Neogene volcano
- Late Ediacaran to Paleozoic units
- Ediacaran Saghro and Ouarzazate Groups (ca. 625-550 Ma)

Figure 1

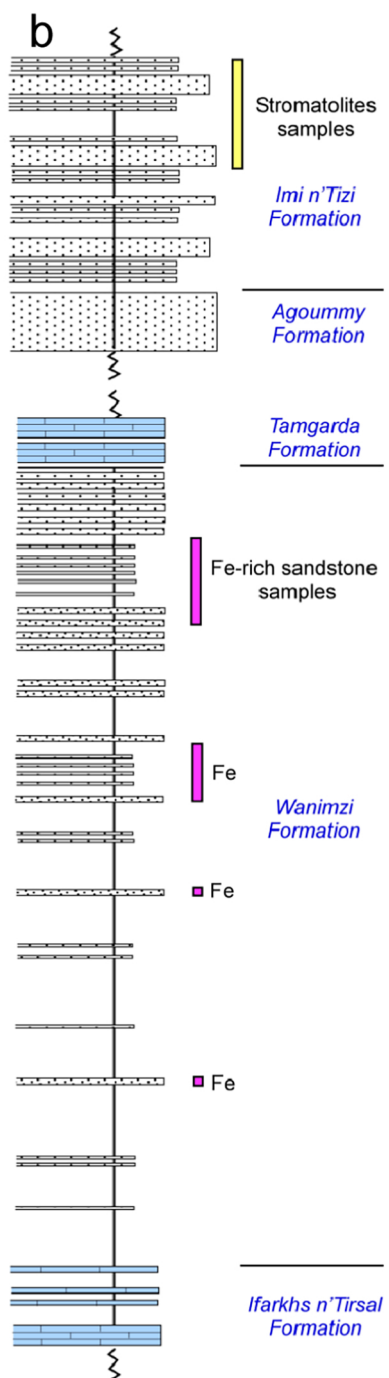
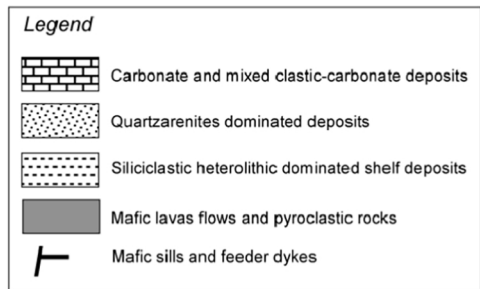
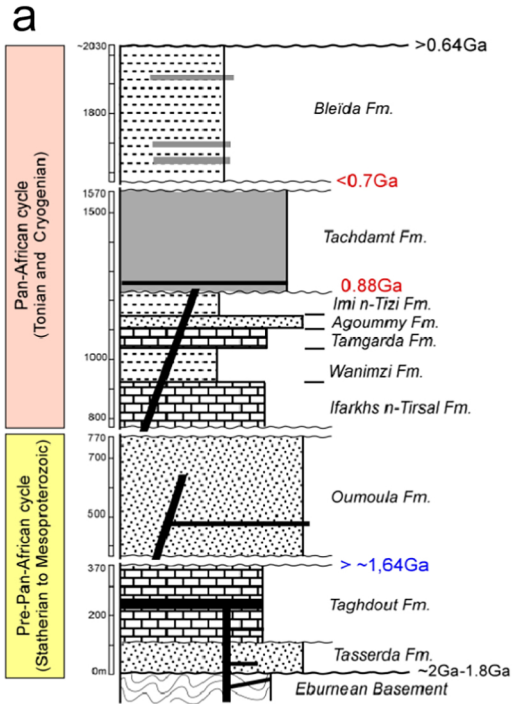


Figure 2

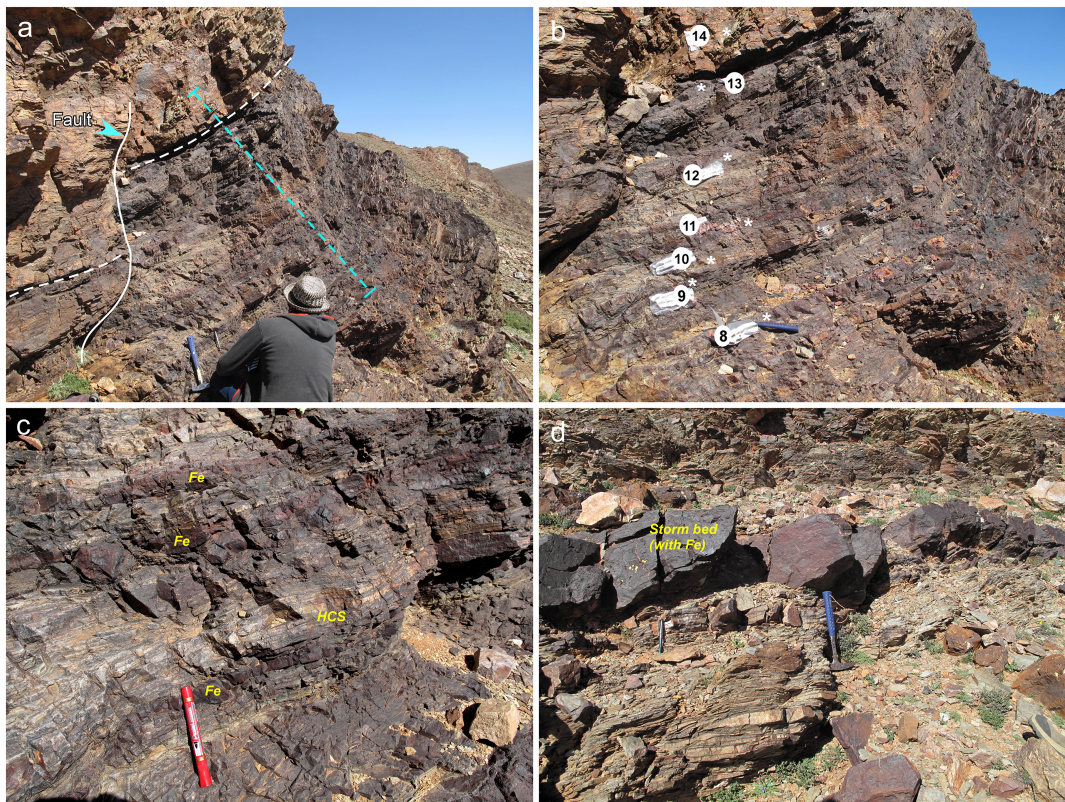


Figure 3

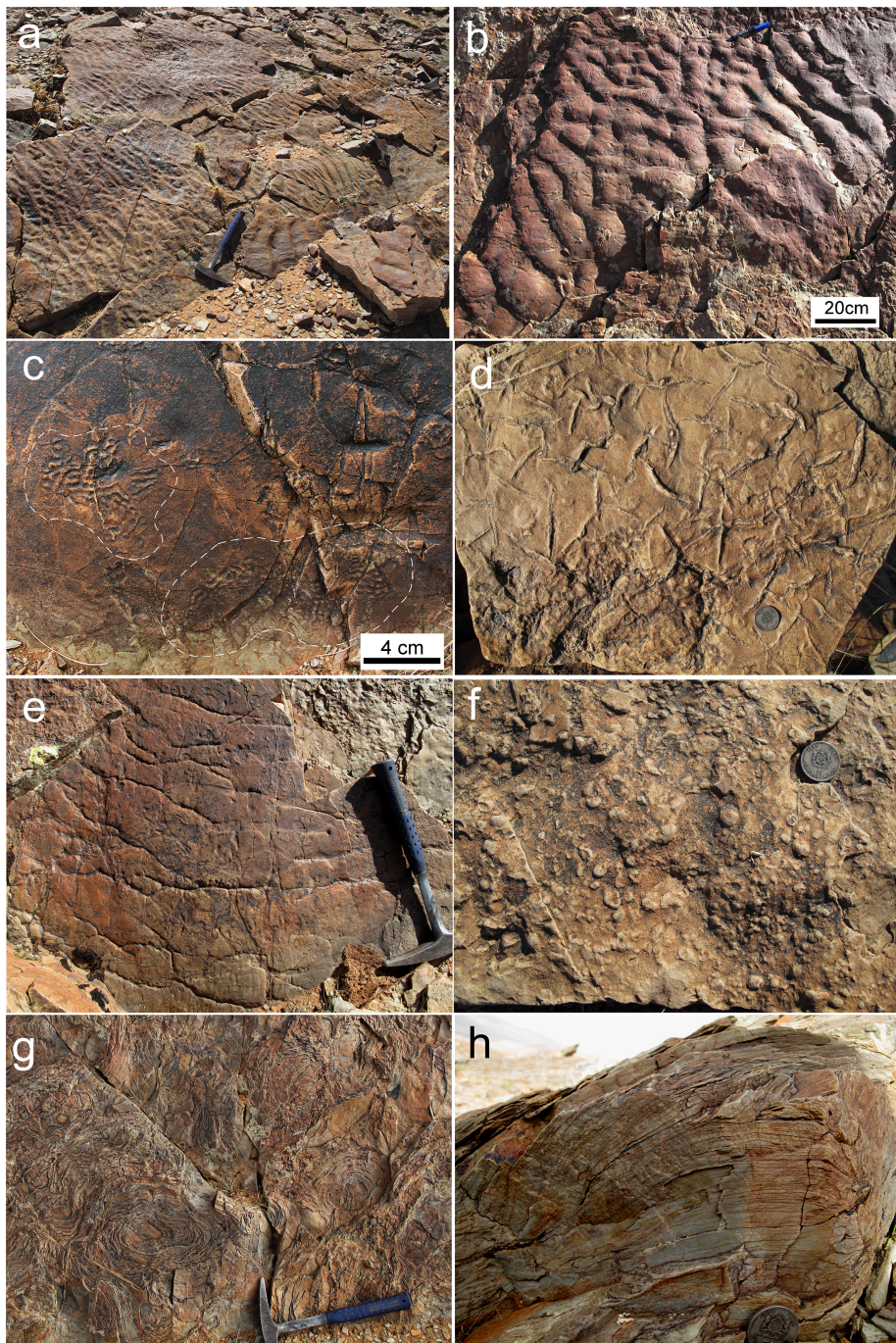


Figure 4

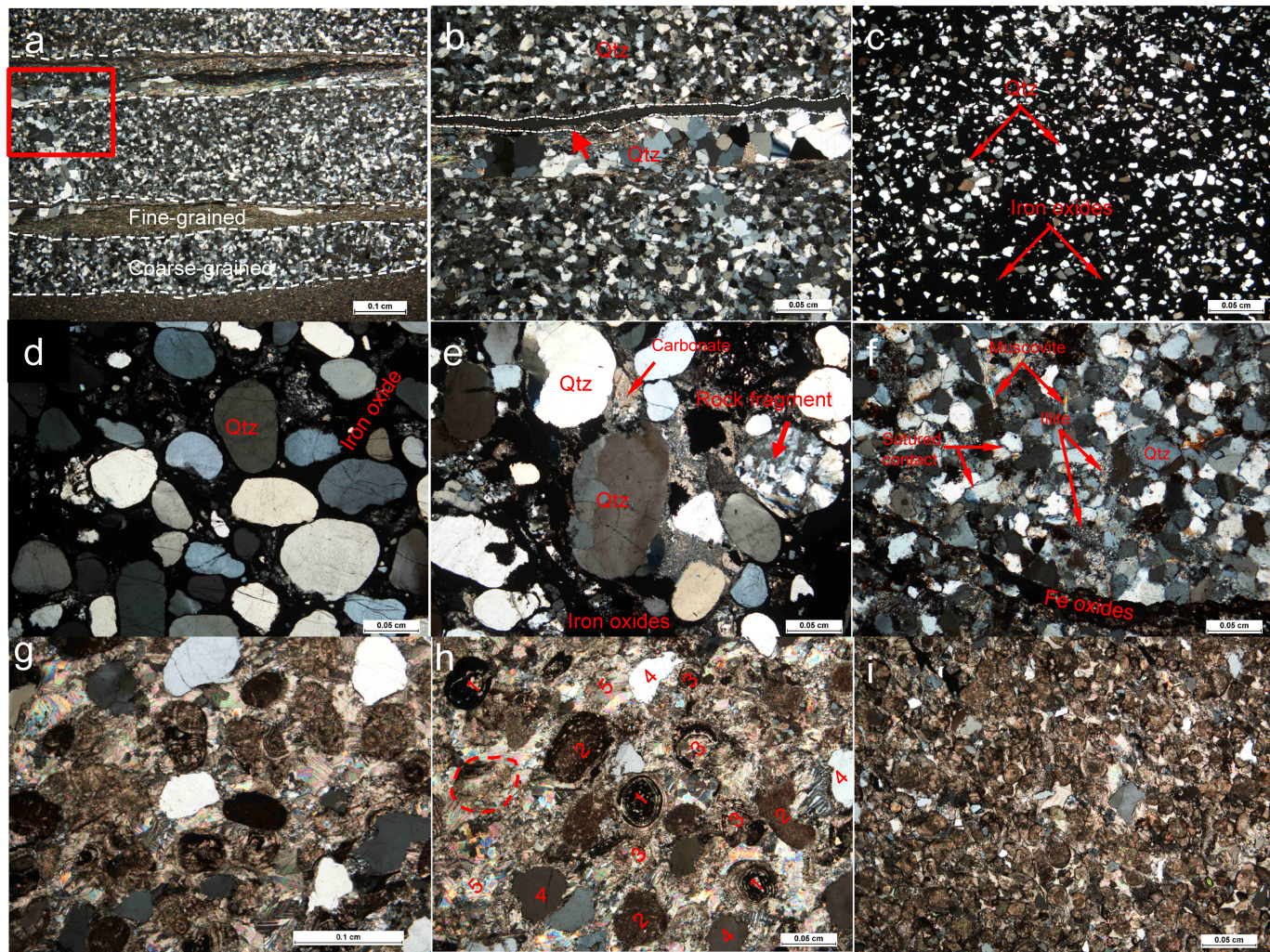


Figure 5

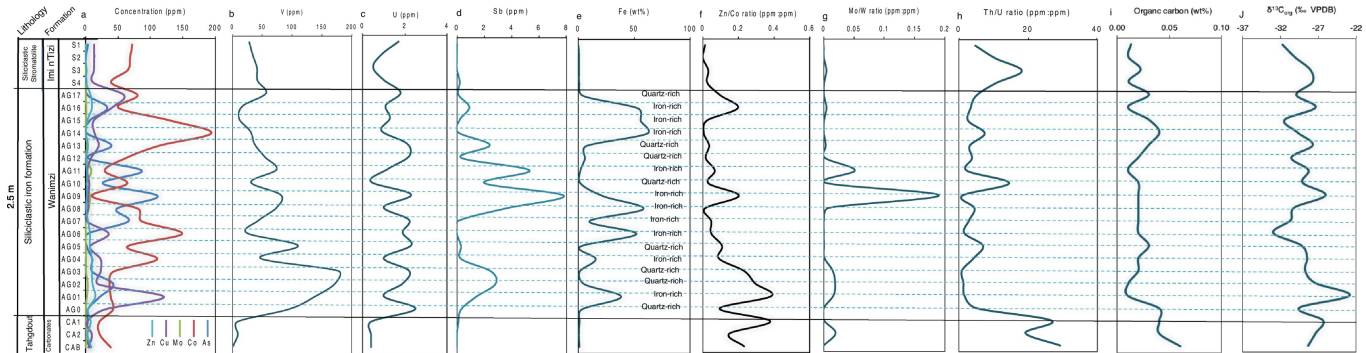


Figure 6

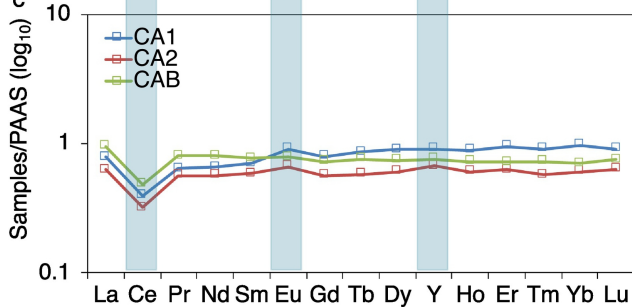
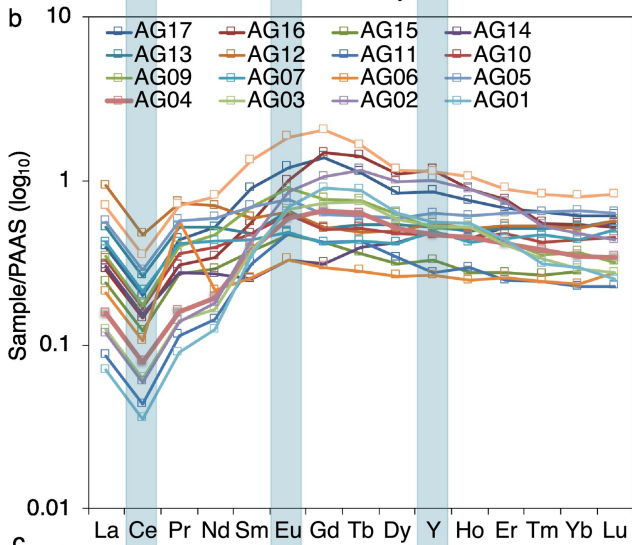
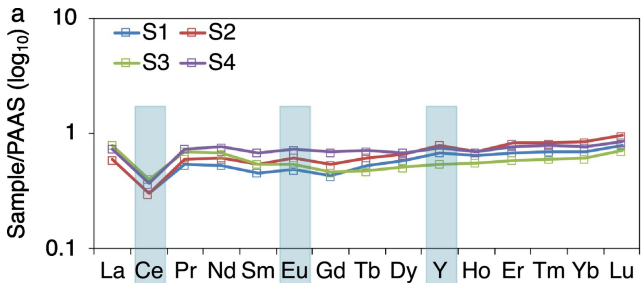


Figure 7

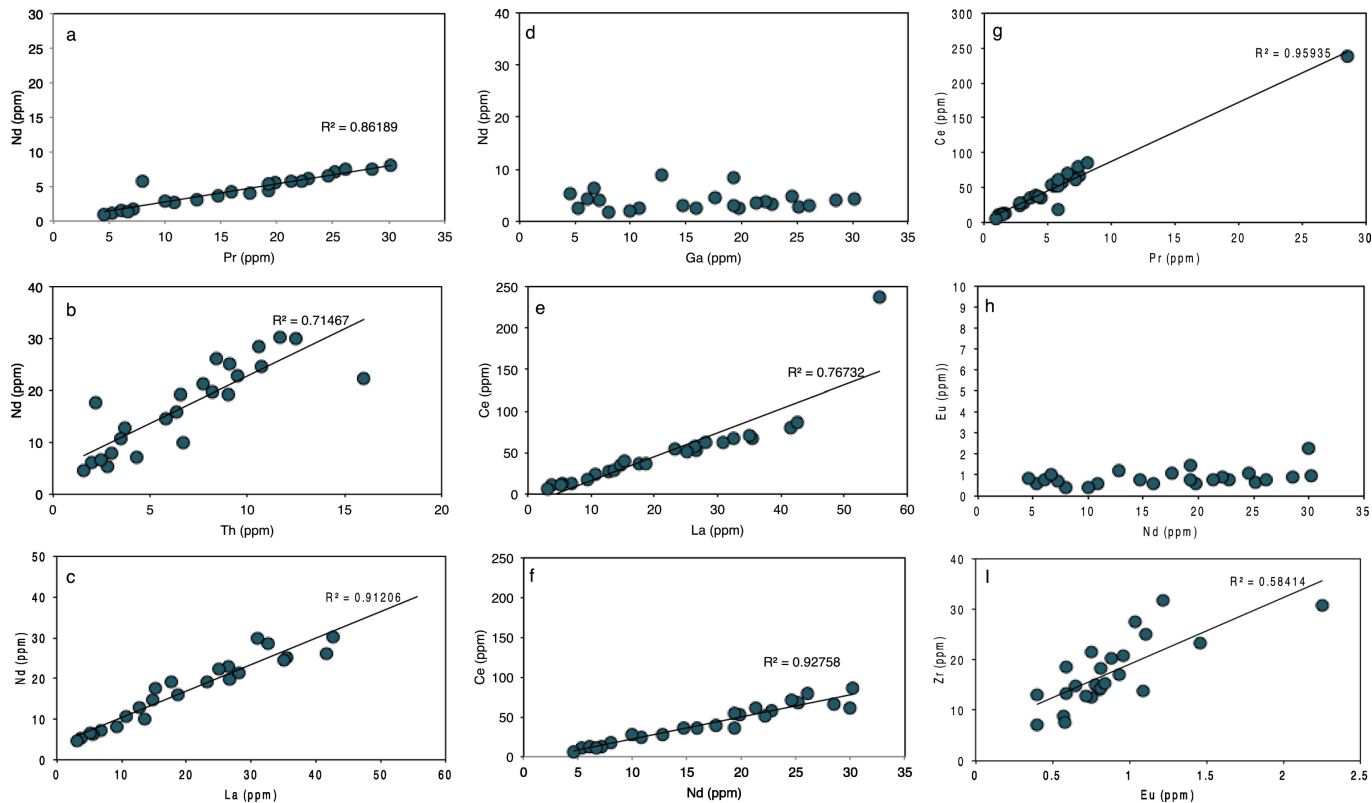


Figure 8

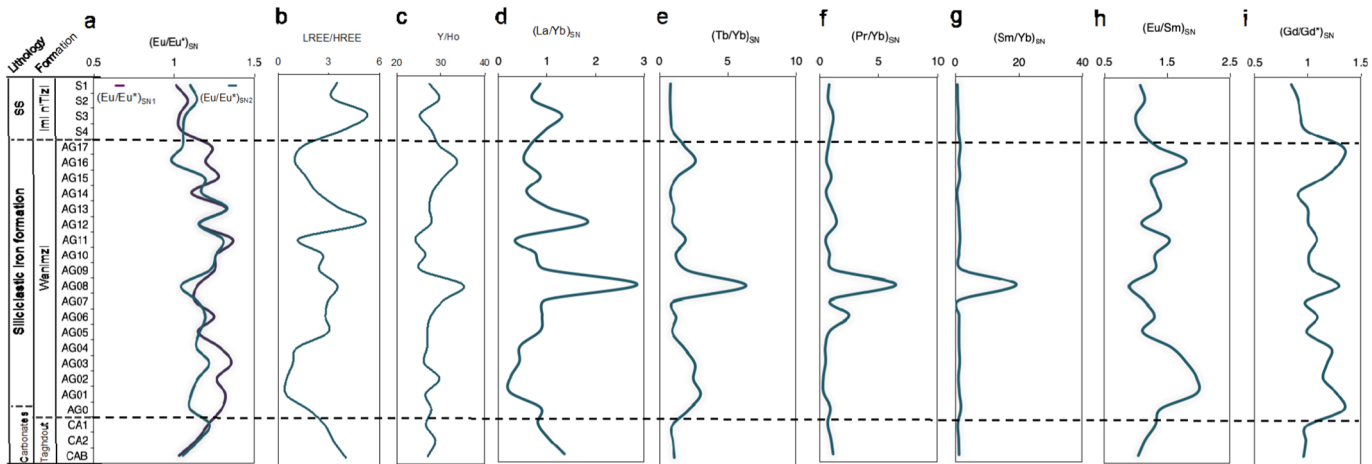


Figure 9

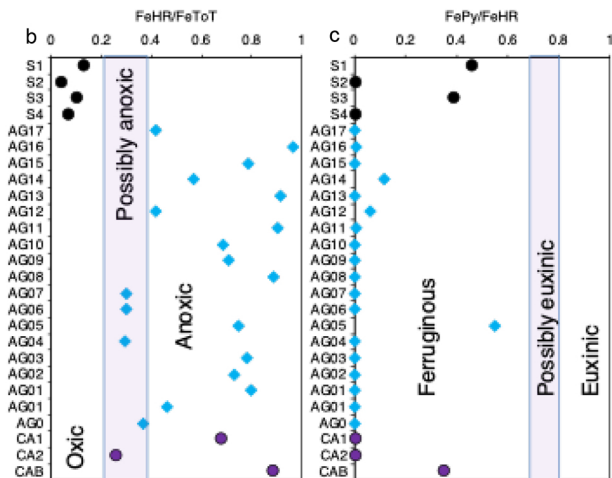
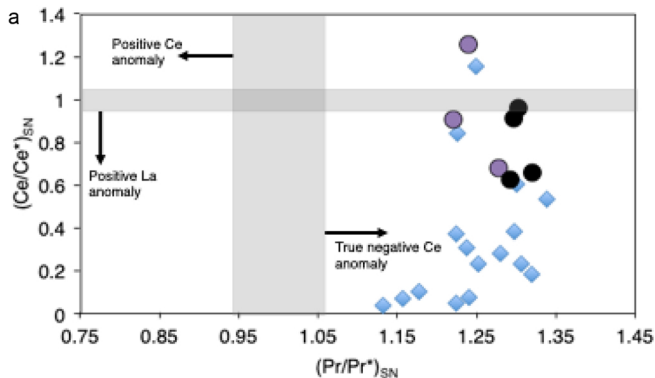


Figure 10

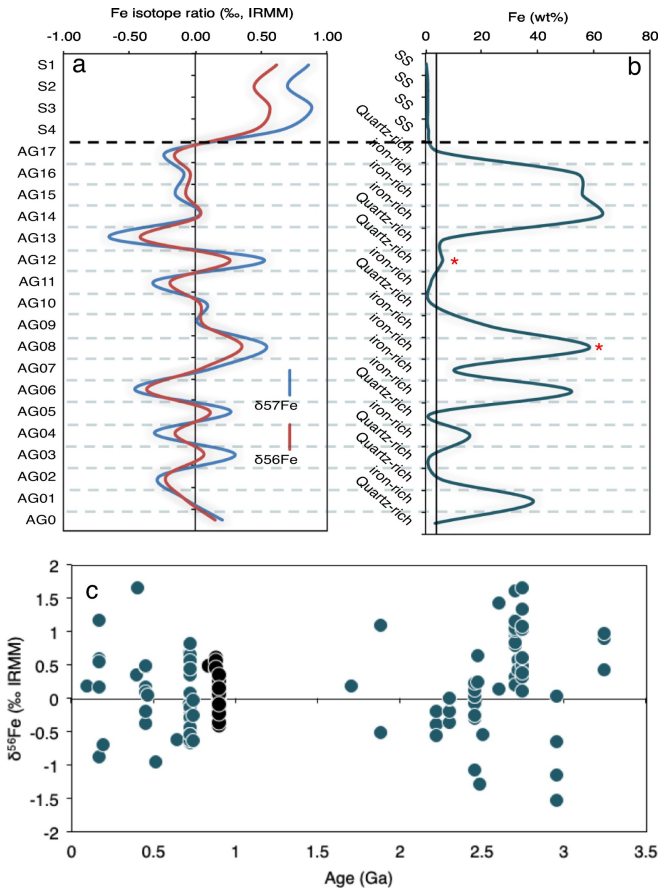


Figure 11

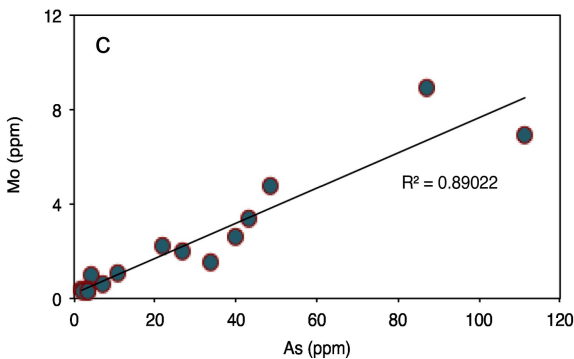
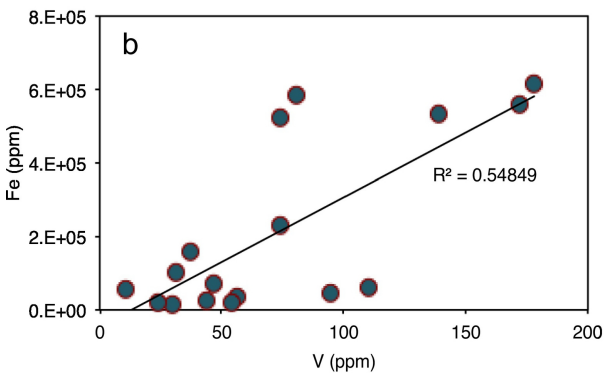
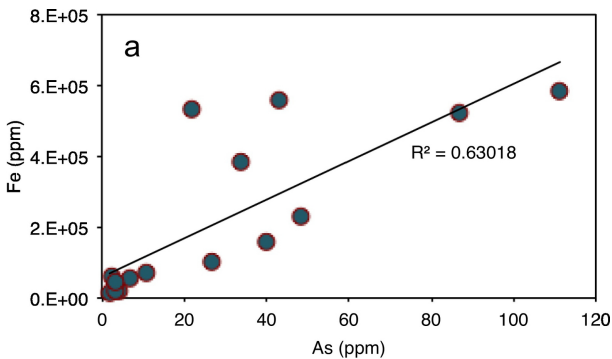


Figure 12

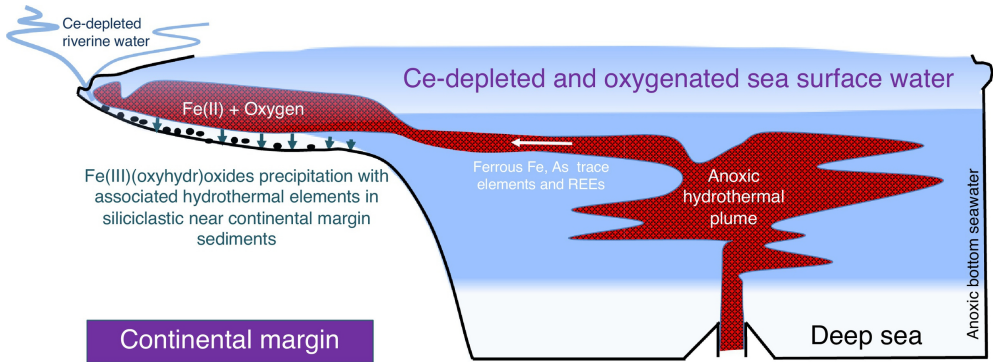


Figure 13